Cell type specificity of neurovascular coupling in cerebral cortex

Abbreviated title: Neuronal types driving dilation and constriction

Hana Uhlirova[1*#], Kıvılcım Kılıç[2*], Peifang Tian[2,3], Martin Thunemann[1], Michele Desjardins[1], Payam A. Saisan[2], Sava Sakadžić[4], Torbjørn V. Ness[5], Celine Mateo[6], Qun Cheng[2], Kimberly L. Weldy[2], Florence Razoux[2], Matthieu Vandenberghe[1,7], Jonathan A. Cremonesi[8], Christopher G.L. Ferri[2], Krystal Nizar[9], Vishnu B. Sridhar[10], Tyler C. Steed[9], Maxim Abashin[11], Yeshaiahu Fainman[11], Eliezer Masliah[2], Srdjan Djurovic[12], Ole A. Andreassen[7], Gabriel A. Silva[10,13], David A. Boas[4], David Kleinfeld[6,11,14], Richard B. Buxton[1], Gaute T. Einevoll[5,15], Anders M. Dale[1,2], Anna Devor[1,2,4]

[1]Department of Radiology, UCSD, La Jolla, CA 92093, USA

[2]Department of Neurosciences, UCSD, La Jolla, CA 92093, USA

[3]Department of Physics, John Carroll University, University Heights, OH 44118, USA

[4]Martinos Center for Biomedical Imaging, MGH, Harvard Medical School, Charlestown, MA 02129, USA

[5]Department of Mathematical Sciences and Technology, Norwegian University of Life Sciences, N-1432 Ås, Norway

[6]Department of Physics, UCSD, La Jolla, CA 92093, USA

[7]KG Jebsen Centre for Psychosis Research, Division of Mental Health and Addiction, Oslo University Hospital and University of Oslo, 0407 Oslo, Norway

[8]Biology Undergraduate Program, UCSD, La Jolla, CA 92093, USA

[9]Neurosciences Graduate Program, UCSD, La Jolla, CA 92093, USA

[10]Department of Bioengineering, UCSD, La Jolla, CA 92093, USA

[11]Department of Electrical and Computer Engineering, UCSD, La Jolla, CA 92093, USA

[12]Department of Medical Genetics, Oslo University Hospital, 0407 Oslo, and NORMENT, KG Jebsen Centre for Psychosis Research, Department of Clinical Science, University of Bergen, 5020 Bergen, Norway

[13]Department of Ophthalmology, UCSD, La Jolla, CA 92093, USA

[14]Section of Neurobiology, University of California, San Diego, La Jolla, CA 92093, USA

[15]Department of Physics, University of Oslo, 0316 Oslo, Norway

* These authors equally contributed to this work

[#]Current address: CEITEC - Central European Institute of Technology, Brno University of Technology and Institute of Physical Engineering, Fac. of Mechanical Engineering, Brno, Czech Republic

Key words: 2-photon microscopy; optogenetic; dilation; constriction; NPY

Corresponding author:

Anna Devor

9500 Gilman Drive MC 0624

La Jolla, CA 92093-0624

Tel: (858) 232 9940

Fax: (858) 822 1753

Email: adevor@ucsd.edu

The authors declare no conflict of interests

Abstract

Identification of the cellular players and molecular messengers that communicate neuronal activity to the vasculature driving cerebral hemodynamics is important for (1) the basic understanding of cerebrovascular regulation and (2) interpretation of functional Magnetic Resonance Imaging (fMRI) signals. Using a combination of optogenetic stimulation and 2-photon imaging in mice, we demonstrate that selective activation of cortical excitation and inhibition elicits distinct vascular responses and identify the vasoconstrictive mechanism as Neuropeptide Y (NPY) acting on Y1 receptors. The latter implies that task-related negative Blood Oxygenation Level Dependent (BOLD) fMRI signals in the cerebral cortex under normal physiological conditions may be mainly driven by the NPY-positive inhibitory neurons. Further, the NPY-Y1 pathway may offer a potential therapeutic target in cerebrovascular disease.

Introduction

In the past decade, the field of cerebral blood flow and metabolism has experienced a paradigm shift with respect to neurovascular coupling mechanisms. An earlier "metabolic" hypothesis postulated that an increase in cerebral blood flow (CBF) in response to increased neuronal activity (a.k.a. "functional hyperemia") was directly related to energetic costs and driven by bi-products of energy consumption (CO_2, lactate, H^+, etc.) (reviewed in (1)). However, a growing body of experimental evidence, including our own, indicates that while molecules produced by increased energy metabolism do have a vasoactive effect, much of the acute CBF response *in vivo* under healthy conditions is driven by vasoactive messengers related to neuronal signaling (for recent reviews see (2-4)). These messengers, released by specific cell types, actively regulate arteriolar diameters – a key control parameter in the CBF response. Thus, activation of specific types of neurons (and potentially astrocytes) as opposed to the undifferentiated spiking or synaptic activity is likely to determine the vascular response.

Previous studies provided evidence for the involvement of both excitatory and inhibitory neurons in CBF regulation. In Pyramidal cells (PCs), activation of N-methyl-D-aspartate (NMDA) receptors has been demonstrated to stimulate release of prostaglandin E2 produced by cyclooxygenase-2 (COX-2) causing an increase in CBF (5, 6). In inhibitory neurons (INs) – that can be further classified into subtypes based on their neurotransmitter/neuropeptide content, shape, and neurophysiological properties (7) – release of neuropeptides and nitric oxide (NO) has been hypothesized to provide a bidirectional CBF control (reviewed in (3)). Indeed, experiments in cortical brain slices have demonstrated that stimulation of INs can cause dilation or constriction of arteriolar segments embedded in the sliced tissue with the polarity of the effect depending on the INs cell type (8, 9). Further, selective optogenetic (OG) stimulation of INs *in vivo* was shown to increase CBF (10).

On the level of single cortical arterioles, two-photon imaging studies have revealed that the hemodynamic response to a sensory stimulus is composed of a combination of dilatory and

constrictive phases with the relative strength of vasoconstriction co-varying with that of neuronal inhibition (11-13). However, direct evidence that activation of INs can cause arteriolar vasoconstriction *in vivo* is missing. Therefore, in the present study, we asked whether selective OG stimulation of INs can cause the biphasic dilation/constriction sequence characteristic of sensory-induced responses and whether the constriction phase was specific to activation of INs rather than excitatory neurons. Our results confirm the ability of INs to drive the biphasic arteriolar response and provide the first *in vivo* evidence for the major role of the NPY-Y1 pathway mediating vasoconstriction.

Results

Sensory stimulation induces arteriolar dilation followed by constriction with the fastest dilation onset below layer IV

Previously, we and others have shown that sensory stimuli in the primary somatosensory cortex (SI) induced biphasic changes in arteriolar diameters – dilation followed by constriction – with the onset and time-to-peak of dilation depending on the cortical depth (13, 14). In these studies, imaging was performed in the rat SI within the top ~500 μm (layers I-IV in the rat SI), and the fastest dilation occurred at the deepest measurement locations. Since infragranular layers V and VI were not sampled, it remains unclear whether sensory-induced dilation initiated in layer IV (which has the highest metabolic load (15)) or below.

In the present study, we extended these measurements down to ~900 μm (layer VI) in the mouse SI (**Figure 1A**). This was possible due to utilization of longer illumination wavelengths (see **Materials and methods**) and higher transparency of the mouse cortex compared to the rat; this is due to smaller diameter of the surface vessels attenuating light. The stimulus consisted of a 2-s train of electrical pulses (100 μs, 1 mA, 3 Hz) delivered to the contralateral forepaw. Fluorescein isothiocyanate (FITC)-labeled dextran was injected intravenously to visualize the vasculature. Single-vessel diameter measurements were performed at 866 locations along 120 diving arterioles and their branches (n = 320 branch measurements) in 49 wild type subjects at depths from 20 to 850 μm. Consistent with our previous data, many of the measurements exhibited a biphasic arteriolar diameter change: dilation followed by constriction before returning to the baseline. To quantify the constriction amplitude, individual time-courses were temporally smoothed with a Gaussian kernel (FWHM = 0.5 s); the peak constriction was determined as the minimum value within 3-13 s after the stimulus onset. About half of the measurements showed constriction with the peak constriction amplitude exceeding 1% (**Figure 1B** and **Figure 1 – figure supplement 1, A**).

To quantify the dilation onset, we fit a straight line to the rising slope of the diameter increase between 20 and 80% of the peak and calculated an intercept with the pre-stimulus baseline for each measured time-course. There was a gradual decrease in the onset and time-to-peak throughout the depth ($P = 1.8x10^{-6}$ and $2.3x10^{-6}$, respectively; **Figure 1C-D**). The dilation amplitude varied between measurement locations (**Figure 1 – figure supplement 1, B-C**).

These results are in agreement with our earlier observations in the rat SI, demonstrating biphasic arteriolar diameter changes with depth-dependent dilation onset and peak. Novel to the present study, these data show that the fastest dilation onset and rise occurs in deep cortical layers, below layer IV.

OG stimulation of INs reproduces the biphasic arteriolar response

We imaged OG-induced single-vessel diameter changes in 17 VGAT-ChR2(H134R)-EYFP mice (16). Double immunofluorescence of ChR2-EYFP and GABA-producing glutamate decarboxylase in this mouse line revealed a virtually complete overlap of staining in the SI confirming that the ChR2-EYFP protein was indeed present only in GABAergic INs (**Figure 2 – figure supplement 1**). The OG stimulus was delivered to the cortical surface through the objective using a cylinder-shaped 473-nm laser beam 230 μm in diameter (FWHM) (**Figure 2A**). Due to significant absorption of light at this (blue) wavelength, the power of the beam was reduced by ~ 90% within the first 200 μm, practically confining the direct effect of ChR2 opening to the top cortical layers (**Figure 2B**). This number, obtained using a Monte Carlo simulation of photon migration in tissue (17, 18), is consistent with previous experimental and theoretical findings (19-21).

FITC-labeled dextran was injected intravenously to visualize the vasculature. We measured 93 diving arterioles within the forepaw area of SI at different depths: from 30 to 560

μm below the cortical surface; 217 measured locations in total. At some locations, lateral branches were captured in the same focal plane within < 200 μm lateral distance from the trunk; 88 branch measurements in total. Sensory stimulation – a 2-s train of electrical pulses (100 μs, 1 mA) delivered to a forepaw at 3 Hz – was presented at one or more measurement locations to control for normal functional hyperemia.

As with the sensory stimulus, the OG stimulus elicited a biphasic vascular response: dilation followed by constriction before returning to the baseline (**Figure 2C-D**). When measured at the same vessel location within the center of the forepaw area, the OG response featured a more pronounced constriction phase compared to the sensory one (**Figure 2D**). The overall shape of the OG response was only weakly sensitive to variation in the light pulse duration (200-430 ms) and intensity (0.7-2.8 mW) (**Figure 2 – figure supplement 2, A-B**). Thereafter, unless indicated, the stimulus consisted of a pair of light pulses separated by 130 ms for 450-ms total stimulus duration. These stimulus parameters produced a robust response while allowing a measurement point in between the two pulses. Averaged within a subject, 16 out of 17 OG time courses exhibited a clear constriction phase (**Figure 2E**). Grouping dilation time-courses by depth revealed that the fastest dilation onset and time-to-peak occurred at the deepest measurement locations (**Figure 2F** and **Figure 2 – figure supplement 2, C**). Indeed, the onset and time-to-peak gradually decreased with depth ($P = 1.2 \times 10^{-3}$ and 4×10^{-5}, respectively; **Figure 2G**). The linear regression slope for the onset was consistent with dilation propagating upstream along diving arteriolar trunks at ~900 μm/s.

Next, we quantified the "constriction onset" as the time of transition from the dilatory to constrictive phase for each measurement location. Constriction onset also gradually decreased with depth ($P = 6.4 \times 10^{-6}$) indicating that deeper dilation had faster decay succeeded by constriction (**Figure 2H**). Deeper measurements exhibited a trend towards higher peak amplitude (**Figure 2 – figure supplement 2, D**). This trend, however, was not statistically

significant due to variation between individual measurements. Finally, presenting the same OG stimulus in wild type animals did not cause any detectable physiological changes (not shown), arguing against potential dilatory/constrictive effects of heat generated by the 473-nm laser within our range of the laser power (22).

Taken together, these results show that selective stimulation of INs was able to reproduce the biphasic dilation/constriction sequence characteristic of sensory-induced responses. As with the sensory responses, the initial OG-induced dilation occurred in deep cortical layers where it also had the fastest rise and fastest decay superseded by constriction.

Vascular response to the OG stimulation of INs does not rely on excitatory cells

In general, an increase in inhibition is expected to hyperpolarize postsynaptic cells reducing their excitability. Hypothetically, however, indirect activation may be produced through disinhibition or generation of a "rebound" action potential upon termination of the hyperpolarization (23). This rebound mechanism is particularly relevant for deep PCs endowed with low threshold calcium conductance (24). To control for these or any other unforeseen effects of the OG stimulation on PC activity, we performed extracellular recordings of the Local Field Potential (LFP) and Multi Unit Activity (MUA) in an additional 3 VGAT-ChR2(H134R)-EYFP subjects (**Figure 3**). LFP in the cerebral cortex largely reflects flow of currents along the vertically aligned PCs' apical dendrites and, therefore, provides a reliable measure of PC activity (25, 26). Our measurements revealed no LFP response timed to the termination of the OG stimulus arguing against the presence of rebound spikes in PCs (**Figure 3A**). In addition, the ongoing (spontaneous) LFP activity was suppressed during the OG stimulus implying the hyperpolarization of PCs. The suppression effect was more obvious during longer OG stimuli (**Figure 3B**).

The MUA signal reflects spiking of all neurons, excitatory and inhibitory, within ~100 μm of the electrode tip (27-29). During the ongoing activity, bursts of MUA coincided with downward

198 deflections in LFP indicating participation of PCs in these spontaneous events. The OG stimulus
199 elicited a sharp and transient increase in MUA timed to the stimulus onset (**Figure 3**). During
200 prolonged OG stimulation, the initial transient MUA response was followed by a desynchronized
201 activity, starting ~200ms after the stimulus onset and lasting for the duration of the stimulus
202 (**Figure 3B**). This MUA response in the presence of LFP suppression suggests firing of INs
203 rather than PCs.

204 To provide further evidence that OG stimulation did not engage PCs, we performed *in*
205 *vivo* calcium imaging in an additional 3 VGAT-ChR2(H134R)-EYFP subjects (**Figure 3 – figure**
206 **supplement 1**). PCs and INs were identified using structural reference images (**Figure 3 –**
207 **figure supplement 1A-B**, see **Materials and methods**). During spontaneous activity, the
208 majority of imaged PCs exhibited characteristic calcium transients known to be associated with
209 action potentials (AP) (**Figure 3 – figure supplement 1C, left**) (30-33). In contrast, calcium
210 transients in INs had variable kinetics and/or small amplitude (**Figure 3 – figure supplement**
211 **1C, right**). Poor quality of calcium signals in INs is consistent with previous reports and is likely
212 to reflect low density of voltage-gated calcium channels and/or higher calcium buffering capacity
213 in INs (34, 35). Therefore, calcium imaging in INs may not provide enough sensitivity for the
214 detection of single (or a few) APs generated by the 5-ms OG stimulus. Indeed, the stimulus
215 produced no detectable calcium increase (**Figure 3 – figure supplement 1C**). To ensure that
216 this stimulus was sufficient to elicit firing, we recorded MUA activity right after acquisition of
217 calcium imaging data. Despite the absence of a calcium increase, there was a robust MUA
218 response to every light pulse (**Figure 3 – figure supplement 1D**). While the calcium imaging
219 experiments failed to detect firing of INs, they provided further evidence that PCs were not
220 activated by OG stimulation. This is because no calcium increase was detected in PCs in
221 response to the OG stimulus, although spontaneous calcium transients were readily detectable.

222 Taken together, these data demonstrate that indirect recruitment of PCs was unlikely to
223 contribute to the OG-induced vascular responses. Furthermore, both the dilation and

constriction phases of the response were present after blocking glutamatergic synaptic transmission with AP5 (NMDA receptor antagonist, 500 μM) and CNQX (AMPA/kainate receptor antagonist, 200 μM) (**Figure 3 – figure supplement 2**, see **Materials and methods**). These results are in agreement with a recent laser speckle contrast imaging study in the same VGAT-ChR2(H134R)-EYFP mouse line, which concluded that the effect of OG stimulation on CBF was independent on synaptic transmission (10). Thus, arteriolar dilation and constriction in response to the OG stimulation was a consequence of direct activation of INs expressing ChR2 with no reliance on excitatory cells.

Neurovascular mechanism induced by the OG stimulation of INs requires spiking

At first glance, the finding that OG-induced dilation initiated below layer IV (**Figure 2F-G**) while the 473-nm light used to deliver the OG stimulus was practically confined to the top 200 μm is puzzling (**Figure 2B**) (20, 21). However, a previous study using OG stimulation of layer V PCs has shown that stimulation at the cortical surface was effective in inducing firing of cell bodies located in layer V (36). Similar to PCs, some subtypes of INs (with bipolar, bitufted, double-bouquet, Martinotti-like morphologies (7)) span across the cortical depth with the top part of their dendritic and/or axonal arbor residing in the upper cortical layers. Therefore, we hypothesized that opening of ChR2 channels in these superficial neuronal processes could be sufficient to cause depolarization throughout the cell triggering release of vasoactive agents below the penetration limit of blue light in tissue, either from axonal terminals or via dendritic exocytosis (37).

The superficial processes undergoing depolarization due to opening of ChR2 could be axons, dendrites, or both. Structural 2-photon imaging in the VGAT-ChR2(H134R)-EYFP mouse showed that EYFP (and, therefore, ChR2) was present in the somas and processes of INs across cortical layers (**Figure 4A**). Each EYFP-positive neuron had a number of processes

emanating from the cell body consistent with the presence of ChR2 in the dendrites. Axonal labeling, however, could not be determined from these data.

First, we examined the possibility of ChR2 opening in the superficial axons. Assuming that ChR2 was indeed present in the axons, we reasoned that depolarization of these axons could be sufficient for triggering antidromic APs (38) coupling the surface illumination to the release of vasoactive messengers in deep layers. In this case, we predicted that the vasoactive effect would be abolished by blocking APs and rescued by delivering the OG light stimulus directly to layer V (i.e., bypassing the need for antidromic APs as the means of communication). To test this hypothesis, we topically applied 50 μM of tetrodotoxin (TTX), a blocker of Na^+ channels required for generation and propagation of APs (n = 3 subjects). TTX abolished both the dilation and constriction response phase at all depths (**Figure 4B**). Next, we used a tapered optical fiber (see **Materials and methods**) positioned with the light-emitting tip ~ 600 μm below the surface (layer V). Under control conditions, OG stimulation through the fiber induced the characteristic biphasic arteriolar response (**Figure 4C**, black curve). In the presence of TTX, however, both the dilation and constriction phase were lost (n = 3 subjects) (**Figure 4C**, red curve).

The failure to rescue the response in the presence of TTX while delivering light directly to layer V argues against antidromic APs as the means of communication between the surface excitation and deep dilation onset. These results also imply that, in the absence of spikes, dendritic depolarization was insufficient to induce vascular responses arguing for release of vasoactive agents from axonal terminals rather than via dendritic exocytosis. In addition, these results indicate that the density of ChR2 in axonal terminals was insufficient to drive the release directly, i.e., due to the depolarization and calcium influx resulting from opening of ChR2 in these terminals. Thus, (1) spikes were required to enable release of vasoactive agents, and (2) the communication of the surface excitation to deep release likely occurred via propagation of

depolarization to along dendrites rather than axons.

The dilation phase is likely to be mediated by bipolar INs with superficial dendrites and deep axons

In contrast to axons that support regenerative propagation of APs, dendritic depolarization decays with distance. Therefore, first we asked whether depolarization of superficial dendrites in INs could, in principle, drive the soma, located in layer V, above its firing threshold. To address this question, we computed membrane potential in morphologically reconstructed INs. Specifically, we chose bipolar INs positive for Vasoactive Intestinal Peptide (VIP). This choice was motivated by the desired orientation of the dendritic and axonal arbors in VIP-positive INs (39) (**Figure 4D** and **Figure 4 – figure supplement 1**) as well as the known vasodilatory properties of VIP (8, 40).

Reconstructed VIP-positive neurons were obtained from the NeuroMorpho.Org (41) (see **Materials and methods**). We computed the membrane potential at the soma in response to a step depolarization ("voltage clamp") of the upper part of their dendritic tree. All computations were carried out in the Neuron simulation environment (42). We assumed passive membrane properties and clamped the voltage of the top 50-, 100- or 150-μm slab of the dendritic tree to 0 mV, which is the reversal potential of ChR2 (43). For all three conditions, we observed a strong depolarization of the soma that developed within ~50 ms. The steady state depolarization reached values between -40 to -50 mV, depending on the number of dendritic branches within the clamped region, comparable to the reported -43.7 mV average firing threshold for VIP-positive neurons (44) (**Figure 4D**). In reality, dendritic membranes of INs possess active ionic conductances (reviewed in (40)) enhancing the coupling of dendritic excitation to generation of spikes. Therefore, our calculation underestimates the achievable somatic depolarization. Thus, we conclude that depolarization of the upper dendrites in bipolar INs can drive spikes in somas located as deep as layer V.

The need to overcome the decay of depolarization along the dendrite implies that OG stimulation delivered directly to layer V should be more effective in inducing the vascular response compared to stimulation from the surface. To test this hypothesis, we made paired measurements in response to stimulation through the objective and fiber (positioned with the light-emitting tip ~ 600 μm below the surface) at each measured location (n = 30 locations along 4 arterioles in an additional 3 subjects, within 50-500 μm depth range). The stimulus consisted of a single light pulse (330-430 ms duration). **Figure 4E** shows the vascular responses, averaged across subjects, for each condition and the corresponding laser power. Normalized by the laser power, the peak dilation in response to the fiber was roughly twice as large as that in response to stimulation through the objective (**Figure 4E**, inset). Thus, initiation of dilation below layer IV in response to OG light at the cortical surface could be explained by depolarization of the superficial dendrites leading to firing of the soma (situated as deep as in layer V) and release of vasoactive agents from deep axons.

The constriction phase is mediated by Y1 receptors for Neuropeptide Y

During the hemodynamic response to a sensory stimulus, the relative strength of arteriolar constriction in SI covaries with that of neuronal inhibition (11, 12). Thus, neurovascular mechanism(s) governing arteriolar constriction may be specific to activation of INs rather than excitatory neurons. To test this hypothesis, we employed Thy1-ChR2-YFP (line 18) mice where expression of ChR2 is limited to layer V PCs (45). Excitation of PCs can engage other cell types because glutamate released from PCs causes depolarization and firing of postsynaptic neurons. For that reason, we applied blockers of glutamatergic synaptic transmission (AP5 and CNQX, see **Materials and methods**) to avoid indirect activation of neuronal cell types other than PCs. Under control conditions, OG stimulation in Thy1-ChR2-YFP mice (using a single light pulse of 50-80 ms duration) elicited a biphasic arteriolar diameter change consisting of the initial dilation followed by constriction (n = 2 subjects, 28 measurement locations along 13 arterioles within 40-

380 μm depth range; **Figure 5A**, black). However, only dilation was observed in the presence of the glutamatergic blockers (**Figure 5A**, red). Thus, indirect activation of postsynaptic neurons accounted for the constriction phase. Taken together with the VGAT-ChR2(H134R)-EYFP data, these results indicate that both INs and PCs could drive dilation while constriction was selective to activation of INs.

Which subtype of INs mediates the constriction phase? Previous studies have demonstrated constriction of cortical arterioles following activation of NPY-positive INs in brain slices and during perfusion of the slice chamber (or isolated vessels) with NPY (8, 9, 46). Further, NPY-Y1 receptors are known to be expressed by cortical microarterioles (47, 48). Motivated by these reports, we tested the effect of a Y1 antagonist BIBP 3226 on the constriction phase of vascular responses elicited by the OG stimulation in 3 VGAT-ChR2(H134R)-EYFP subjects. Topical application of 100 μM of the antagonist largely abolished the constriction phase of the OG response without a significant effect on the peak dilation amplitude (n = 52 locations along 25 diving arterioles at depths from 50 to 590 μm) (**Figure 5B**).

Next, we tested the effect of the same pharmacological treatment on dilation in response to the sensory stimulus. Sensory stimulus-induced dilation was measured at 10 locations along 7 diving arterioles in 4 additional wild type subjects at depths from 130 to 490 μm. At each location, measurements were performed before and after the topical application of 100 μM of BIBP 3226. **Figure 5C** shows the averaged time-courses before and after BIBP 3226 (black and red, respectively). For vessels exhibiting a clear biphasic response, the constriction phase was abolished by BIBP 3226 without a significant effect on the peak dilation amplitude (**Figure 5C**, left). For vessels exhibiting monophasic dilation, there was a trend towards higher dilation amplitude after BIBP 3226 (**Figure 5C**, right). This trend, however, was not significant.

These results are consistent with prior demonstrations in brain slices that dilation and constriction are mediated by different types of INs (3, 8, 9). We conclude that the constrictive

effect elicited by both the OG and sensory stimuli was driven by NPY – presumably released from NPY-positive INs (49) – acting on Y1 receptors.

Biphasic arteriolar response to sensory and OG stimuli in the absence of anesthesia

Anesthesia can differentially affect neuronal cell types altering neuronal network activity and neurovascular coupling. To this end, we performed 2-photon imaging of single diving arterioles in awake mice, i.e., in the absence of general anesthesia or any sedative drugs (see **Materials and methods**). The sensory stimulus consisted of three gentle air puffs onto the whisker pad (100-ms puffs delivered at 3 Hz). Diving arterioles within the whisker pad representation of SI (i.e., Barrel cortex) displayed readily detectable biphasic arteriolar responses to the sensory stimuli consisting of dilation followed by a smaller amplitude constriction (n = 4 subjects, 11 measurement locations along 11 arterioles within 30-120 μm depth range; **Figure 6A** top, black). The overall response duration was shorter than that in the anesthetized subjects (**Figure 1B**), most likely due to differences in the stimulus duration and strength (1-s train of air puffs in awake vs. 2-s train of electrical pulses under anesthesia). In addition, awake subjects exhibited a secondary dilation of smaller amplitude 10-15 s after the stimulus onset, likely reflecting cognitive processing and, in some cases, active whisking following the sensory stimulus.

Next, we performed measurements in awake VGAT-ChR2(H134R)-EYFP subjects in response to OG stimulation of INs (n = 3 subjects, 11 measurement locations along 10 arterioles within 30-120 μm depth range; **Figure 6A** bottom, red). The stimulus consisted of a single light pulse (150-400 ms duration). Similar to the response under anesthesia, the OG stimulus induced biphasic arteriolar diameter changes with more pronounced constriction compared to the sensory response (**Figure 6B**). These results rule out the possibility that the

constriction phase could be an epiphenomenon of anesthesia establishing the biphasic dilation/constriction sequence as a normal feature of the hemodynamic response at the level of parenchymal arterioles.

Discussion

A key goal in neurovascular research is establishing molecular mechanisms mediating dilation and constriction of the brain microvasculature driven by changes in neuronal activity. In the present study, we used optogenetics to isolate the mechanisms originating from the inhibitory (GABAergic) population of cortical neurons. We demonstrate that OG stimulation elicited a biphasic diameter change composed of a combination of dilatory and constrictive phases. While dilation was also induced by OG stimulation of PCs, the constriction response was specific to activation of INs. Further, we identified the vasoconstrictive molecular agent as NPY acting on Y1 receptors and showed that the same NPY-Y1 pathway was responsible for the sensory stimulus-induced vasoconstriction. This finding supports previous observations in brain slices implicating NPY-positive INs as the primary mediators of vasoconstriction in cortical arterioles under normal conditions (8, 9).

Previously, we reported the center-surround and contra-ipsilateral patterns of arteriolar diameter changes in SI in response to a sensory stimulus that were dominated by dilation within the receptive field and constriction in the surrounding region as well as in the ipsilateral to the stimulus hemisphere (11, 12, 50). The strength of constriction in these studies correlated with the strength of inhibition. In contrast to natural behavior of cortical circuits where specific types of INs play a differential role in “local” and “lateral” inhibition (51), OG stimulation of INs in the present study produced indiscriminate activation across various inhibitory cell types. Therefore, arteriolar responses to the OG stimulation cannot be directly compared to the results from these previous studies. However, the finding of the NPY-Y1 pathway underlying constriction predicts that NPY-positive INs may be specifically involved in shaping the surround and ipsilateral neuronal inhibition.

OG stimulation in the VGAT-ChR2(H134R)-EYFP line produced a monophasic CBF increase in a recent laser speckle contrast imaging study by Anenberg et al. (10). Arteriolar constriction, however, would normally result in a CBF decrease, as we demonstrated previously (11, 12). We speculate that the high-frequency stimulation protocol used by Anenberg and colleagues may have contributed to the lack of constriction and CBF decrease in their study. In contrast to other types of INs driving dilation, at least some NPY-positive neurons exhibit a pronounced spike latency (49) and thus may not respond well to short (5-ms duration) light pulses delivered at high frequency (100 Hz).

Prior studies on neuropeptides in different brain areas have demonstrated that the release could occur from axonal terminals as well as via dendritic exocytosis (37). In the present study, OG stimulation of ChR2-expressing dendrites and somas under TTX was not effective in causing vascular responses while delivering the stimulating light either to the cortical surface or deep layers. These results suggest that the corresponding vasoactive agents, including NPY, were released from axons rather than via dendritic exocytosis, while spikes were required to drive the release. Yet, we cannot rule out a possibility of dendritic release induced by back-propagating APs (52). Indeed, back-propagating APs have been reported in bipolar, bitufted and neurogliaform INs (53-55).

The requirement for spiking during the OG response should not be interpreted in the context of the “classical” question of whether it is the spiking or synaptic activity that correlates better with BOLD fMRI. Historically, this question was motivated by the idea of a metabolic feedback, postulating that CBF increase was mechanistically related to the accumulation of vasoactive energy metabolites (1). The present results, on the other hand, demonstrate a feed forward mechanism where specific vasoactive signaling agents released by active neurons drive dilation and constriction, depending on neuronal cell type. Further, the initial dilation in our experiments occurred in infragranular layers and not in layer IV, which is the most metabolic layer in SI (15). These findings do not contradict the fact that some of the energy metabolites

are vasoactive (56). Rather, they suggest that, under healthy conditions *in vivo,* it is the vasoactive messengers related to neuronal signaling and not energy metabolites that play the dominant role in CBF regulation.

The identity of vasodilatory mechanisms induced by OG stimulation of INs requires further investigation. Previous studies put forward a number of possibilities including release of VIP and NO (3, 57). The present results indicate that INs mediating dilation may have bipolar morphologies with dendrites extending to the surface and axons reaching to deep cortical layers. VIP-positive INs meet these morphological criteria, and some of them co-express neuronal nitric oxide synthase (39, 40, 58). These features as well as known vasodilatory properties of VIP (8, 40) put forward VIP-positive INs as a primary suspect initiating dilation in deep layers. Future experiments using restricted expression of OG actuators/inhibitors in sub-populations of INs with known repertoire of vasoactive signaling molecules would be required to comprehensively address this hypothesis.

It is well established that dilation and constriction can propagate along arteriolar walls (59-64), and these conducted responses may have contributed to the spread of OG dilation and constriction throughout the cortical depth in our data. This possibility is consistent with the observed slowing down of dilation kinetics towards the cortical surface and the trend towards a gradual decrease in the peak amplitude – this type of behavior is expected for a decaying propagated response (65, 66). These findings, however, do not imply that neurovascular coupling mechanisms reside exclusively in deep cortical layers and do not rule out local lamina-specific neurovascular communication at every depth. In the presence of both local and conducted signaling, the onset of dilation would be determined by the faster of the two processes. Therefore, substantial delays in the superficial arteriolar branches suggest that local neurovascular communication in the upper layers, if it exists, has slower kinetics.

The observed gradual decrease of the dilation latency and time-to-peak down to the infragranular layers is in agreement with laminar resolved functional Magnetic Resonance

Imaging (fMRI) in human (67) but at odds with a recent high resolution fMRI in the rat that used a line-scanning method (68). The apparent discrepancy with Yu et al. (2014) may reflect the complex nature of the Blood Oxygenation Level Dependent (BOLD) fMRI signal that depends on the balance between O_2 delivery and consumption as well as on the measurement theory specific to the chosen data acquisition paradigm. Our present conclusions, on the other hand, rely on direct and assumption-free measurements of the physiological parameter of interest – the arteriolar diameter.

Astrocytic contribution to either dilation or constriction evoked by the OG stimulation of INs was not specifically addressed in the current study. A number of recent reports including our own have provided negative evidence for the involvement of calcium-dependent release of vasoactive gliotransmitters in normal regulation of cortical blood flow by local neuronal activity (69-72). However, we cannot rule out calcium-independent pathways. Expression of Y1 receptors has been documented in astrocytic cultures (47); although, more recent transcriptomic analyses of astrocytes isolated from adult mouse brains have revealed little or no expression of these receptors (73, 74).

The present study has a number of limitations. As such, the pattern of OG stimulation in space and time did not mimic naturally occurring neuronal activity. In addition, the possible variation in the level of ChR2 expression could have resulted in bias towards specific INs cell types. The design of our OG study, however, did not rely on natural or balanced neuronal activity patterns. Instead, our major goal was to produce artificially selective activation of cortical INs as a single population for isolation of their vasoactive effects. Another potential pitfall is that OG stimulation of INs could lead to an indirect recruitment of PCs, which have been implicated in regulation of blood flow (6). However, our electrophysiological recordings and calcium imaging data produced no evidence for PC recruitment. Finally, the majority of the experiments in our study were performed under anesthesia and in the presence of a paralytic agent that could have affected the vasoreactivity and neurovascular coupling. As such, the

ketamine/xylazine anesthesia employed by Anenberg et al. (10) may provide an additional explanation for the discrepancy in our results regarding the constriction phase in response to OG stimulation of INs. Stepping away from anesthesia is an ongoing effort in many laboratories, including our own, but still remains a challenge for studies that require pharmacological manipulations, insertion of recording electrodes, and deep imaging. In the present study, we have confirmed the biphasic nature of the arteriolar diameter change in awake mice, both in response to a sensory stimulus and OG activation of INs.

The constrictive effect of INs demonstrated in the present study, taken together with previous theoretical calculations suggesting that inhibition has lower metabolic costs than excitation (75, 76), raises the possibility that paired CBF and cerebral metabolic rate of O_2 ($CMRO_2$) measurements can provide information about the net respective contributions of excitatory and inhibitory activity within the ensemble neuronal network response, due to their differential vasoactive role and energetic costs. This possibility is of particular interest for the quantitative BOLD fMRI approach (a.k.a. the “calibrated BOLD”) that combines the BOLD and arterial spin labeling (ASL) methods to isolate the effects of CBF and $CMRO_2$ (77-79). Thus, we are tempted to speculate that identifying the CBF and $CMRO_2$ effects induced by excitatory and inhibitory neurons could open a new direction in which quantitative fMRI may be able to provide information on the underlying neuronal activity.

Materials and methods

Animal procedures for imaging under anesthesia

All experimental procedures were performed in accordance with the guidelines established by the UCSD Institutional Animal Care and Use Committee (IACUC). We used 103 adult mice of either sex including 48 VGAT-ChR2(H134R)-EYFP and 2 Thy1-ChR2-YFP (using promoters from *Slc32a1* and *Thy1* genes, respectively; Jackson Stock Numbers 014548 and 007612, respectively; both heterozygous on a mixed C57Bl6/ICR background), and 53 wild type ICR. Surgical procedures in mice expressing ChR2 were performed in a dark room using a 515 nm longpass filter (Semrock FF01-515/LP-25) in the surgical microscope light source to avoid OG stimulation during installation of the cortical window. Mice were anesthetized with isoflurane during surgical procedures (2% initially, 0.5–1% during all procedures). A cannula was inserted into the femoral artery. A metal holding bar was glued to the temporal bone for immobilization of the head during imaging. An area of skull overlying the forepaw region of the primary somatosensory cortex (SI) contralateral to the holding bar was exposed and dura mater removed. A ~2x2 mm cranial window was centered on stereotactic coordinates: AP -0.5, ML 2.25.

In the majority of experiments, the red fluorescent dye sulforhodamine 101 (SR101, S7635, Sigma) in artificial CSF (ACSF) was applied topically for ~2 min to label astrocytes (80) providing a contrast in tissue that was used for visual assessment of potential damage due to experimental procedures. ACSF contained 142 mM NaCl, 5 mM KCl, 10 mM glucose, 10 mM HEPES, 3.1 mM $CaCl_2$, 1.3 mM $MgCl_2$, pH 7.4. The excess dye was washed with ACSF. A drop of agarose (1% wt/vol, A9793, Sigma) in ACSF was applied on the brain surface, and the exposure was covered with a round glass coverslip (5 mm, WPI) and sealed with dental acrylic. To avoid herniation of the exposed brain due to excessive intracranial pressure, the dura mater over the IVth cerebral ventricle was punctured, thus allowing drainage of CSF. After the exposure was closed, the drainage hole was sealed with agarose.

In experiments involving pharmacological manipulations, calcium imaging, or insertion of an optical fiber, the round glass coverslip was cut straight on one side facing a gap in the dental acrylic seal. The agar was cut down along the cut side forming a vertical wall. The exposure was aligned with the agar wall such that ACSF under the objective was in direct contact with the cortical surface allowing drugs to penetrate into the cortical tissue.

After closing of the exposure, mice were left to rest under 1% isoflurane for 45 min. Then, isoflurane was discontinued and anesthesia maintained with α-chloralose (50 mg/kg/h IV, C0128, Sigma or 100459, MP Biochemicals). Mice were paralyzed with pancuronium bromide (0.4 mg/kg/h IV, P1918, Sigma) (81) and ventilated (~110 min^{-1}) with 30% O_2 in air. Fluorescein isothiocyanate (FITC)-labeled dextran (MW = 2 MDa, FD-2000S, Sigma) was injected IV (50-100 μl of 5 % (w/v) solution in phosphate-buffered saline) to visualize the vasculature and control for the integrity of capillary bed. Expired CO_2 was measured continuously using a micro-capnometer (Cl240, Columbus instruments). Heart rate, blood pressure, and body temperature were monitored continuously. Blood gas was analyzed to cross-validate the micro-capnometer measurements. Respiration was adjusted to achieve $PaCO_2$ between 30 and 40 mmHg and pH between 7.35 and 7.45. α-chloralose and pancuronium in 5% dextrose saline were supplied through the femoral line every 30 min for the duration of data acquisition. Waiting for 45 min between closing of the exposure and drug injections minimized leakage of the drugs onto the exposed cortical tissue through the cut dural blood vessels.

For calcium imaging experiments, calcium indicator Oregon Green 488 BAPTA-1 AM (OGB1) (O-6807, Invitrogen, 50 μg) was first dissolved in 4 μl of 20% pluronic in DMSO (F-127, Invitrogen); 80 μl of ACSF were added to the OGB1 solution to yield a final concentration of 0.5 mM OGB1. The microinjection pipette was guided under the glass coverslip and positioned ~ 200 μm below the cortical surface using a Luigs & Neumann translation stage (380FM-U) and manipulation equipment integrated into the Ultima system. The red fluorescent dye Alexa 594

552 (A-10442, Alexa Fluor 594 hydrazide, sodium salt, Invitrogen) was added to the OGB1 solution
553 in order to visualize the micropipette during manipulation and to provide visual feedback during
554 pressure-microinjection into the cortical tissue (33). The pressure was manually adjusted to
555 ensure visible spread of Alexa 594 while avoiding movement artifacts.
556
557 **Animal procedures for imaging awake mice**
558 We used a Polished, Reinforced Thinned-Skull (PoRTS) technique (82) for installation of
559 chronic "cortical windows" providing sufficient visibility for imaging of diameter changes in single
560 diving arterioles down to ~120 μm below the surface. During the PoRTS procedure, mice were
561 anesthetized with isoflurane (2% initially followed by 1% during the surgery); their body
562 temperature was maintained at 37^{o}C. A custom holding bar allowing repeated head
563 immobilization was glued to the skull overlaying the left hemisphere. On the right side, a ~ 3x3
564 mm area of skull was thinned until translucent and polished with silicon carbide grit powder
565 (Convington Engineering). The exposure was centered on the Barrel cortex region of SI using
566 stereotactic coordinates: AP -1.5, ML 2. A glass coverslip was glued to the thinned skull and
567 fixed along the perimeter with dental acrylic. Additional dental acrylic was applied around the
568 holding bar joining to the perimeter of the coverslip in order to reinforce the overall assembly.
569 After surgical implantation of the bar and a full day recovery, mice were habituated in 1
570 session/day to accept increasingly longer periods of head restraint under the microscope
571 objective (up to 2 hrs). During the head restraint, the animal was placed on a suspended bed. A
572 drop of sweetened condensed milk was offered every 15 min during the fixation as a reward.
573 Habituated head-fixed mice consumed the reward milk. They were free to readjust their body
574 position and from time to time displayed natural grooming behavior. A video camera (Lifecam
575 Studio, Microsoft; IR filter removed) with an NIR longpass filter (Midwest Optical LP920-25.5)
576 was used for continuous observation of the mouse. The IR illumination (M940L3 - IR (940 nm)
577 LED, Thorlabs) was invisible for the PMT photodetectors and generated no imaging artifacts.

The camera frames were synchronized with 2-photon imaging and recorded. Periods with extensive body movement (e.g., grooming behavior) were excluded during data analysis.

Sensory stimulation

In experiments under anesthesia, sensory stimulation was delivered to the forepaw contralateral to cortical exposure through a pair of thin needles inserted under the skin using a train of six 100-μs, 1-mA electrical pulses at 3 Hz. This stimulus paradigm was chosen because it produced synchronized neuronal spiking response accompanied by robust dilation with a sharp onset (11, 13, 69). All measurements in response to the sensory stimulus were performed within a 1-mm radius from the center of the forepaw region of SI determined by the stereotactic coordinates (AP -0.5, ML 2.25). Ten stimulus trials were average at each measurement location.

In awake mice, sensory stimulus consisted of a train of three air puffs onto the whiskers contralateral to the cortical window. We used three 100-ms puffs at 3 Hz delivered through a plastic tube (2 mm inner diameter). The tube was positioned behind the whiskers to minimize the eye blink reflex. Seven to nine stimulus trials were average at each measurement location.

Stimulation devices (A365 stimulus isolator or PV830 picopump, WPI) were triggered using a separate PC that also acquired timing signals for data acquisition ("trigger out" signals for each frame/line) and physiological readings using a National Instruments IO DAQ interface (PCI-6229) controlled by custom-written software in MATLAB (MathWorks Inc.). The timing of each frame/line relative to the stimulus onset was determined during data analysis based on acquired triggering signals.

OG stimulation

OG stimulation was delivered though the objective using a 473-nm cylinder-shaped laser beam ~230 μm in diameter (FWHM) (**Figure 2A-B**) that is comparable to the size of a cortical column. The spatial distribution of the photon density in tissue produced by the OG beam

(**Figure 2B**) was estimated using Monte Carlo simulation of photon migration in tissue (17, 18) assuming the following cortical gray matter optical parameters at 473 nm: absorption coefficient μ_a = 0.2 mm^{-1}, scattering coefficient μ_s = 68 mm^{-1}, and anisotropy factor g=0.95 (83). The beam was centered on a diving arteriole using a dedicated set of galvanometer mirrors. The duration of the light pulse was controlled by a dedicated shutter and synchronized with imaging. Only a single OG trial was presented at each measurement location to avoid overstimulation.

In some experiments, the 473-nm beam was coupled to a tapered optical fiber inserted in the cortical tissue (84). Tapered optical fibers were purchased from Nanonics Imaging Ltd. (MM-UV fiber for 200-1200 nm wavelengths, core diameter 50 μm, cladding diameter 125 μm, 250 μm protective acrylate buffer coating (except 2-3 mm from the tip), core refractive index 1.464, cladding refractive index 1.447, numerical aperture 0.22, taper angle between 3^o and 6^o, Cr-Au reflective coating thickness 300 nm, aperture diameter at taper tip ~ 200 nm).

Tapering of the fiber was critical to minimize tissue damage during penetration (84). To generate a larger "blob" of light in deep cortical layers while retaining the needle shape necessary for smooth penetration, we etched 200 μm of the coating from the tip (custom modification by Nanonics). The resultant beam profile is shown in **Figure 4C**. The fiber was guided under the glass coverslip and positioned using Luigs & Neumann translation stage (380FM-U) and manipulation equipment integrated into the Ultima system.

Two-photon imaging

Images were obtained using an Ultima two-photon laser scanning microscopy system from Bruker Fluorescence Microscopy (formerly Prairie Technologies) equipped with an Ultra II femtosecond Ti:Sapphire laser (Coherent) tuned between 800-1000 nm. For penetration deeper than ~ 600 μm, an Optical Parametric Oscillator (Chameleon Compact OPO, Coherent), pumped by the same Ti:Sapphire laser, was tuned to 1360 nm. The OPO was used in

conjunction with the intravascular administration of dextran-conjugated Alexa Fluor 680 (D34680, Invitrogen) (85). FITC and Alexa Fluor 680 were imaged using cooled GaAsP detectors (Hamamatsu, H7422P-40). SR101 was imaged using a multialkali PMT (Hamamatsu, R3896).

In experiments involving OG stimulation, the main dichroic mirror contained a 460-480 nm notch (Chroma ZT470/561/NIR TPC). An additional filter blocking wavelengths in the range 458-473 nm (Chroma ZET458-473/561/568/NIR M) was added in front of the PMT block. Nevertheless, residual bleed-through of the 473-nm light prevented us from using GaAsP detectors. Therefore, in these experiments, FITC (or OGB1) and SR101 were imaged using a pair of multialkali PMTs.

We used a 4x objective (Olympus XLFluor4x/340, NA=0.28) to obtain low-resolution images of the exposure. Olympus 20x (XLUMPlanFLNXW, NA=1.0) and Zeiss 40x (IR-ACHROPLAN, NA = 0.8) water-immersion objectives were used for high-resolution imaging. In experiments involving manipulation of a micropipette or optical fiber under the coverslip, we used a combination of Zeiss 5x (Plan-NEOFLUAR, NA=0.16) and Olympus 20x (UMPlanFI, NA=0.5) objectives for a coarse approach and fine manipulation under the glass coverslip, respectively. The laser beam diameter was adjusted to overfill the back aperture. Diameter measurements were performed in a frame-scan mode at 10-20 Hz, or in a “free-hand” line-scan mode with a scan rate of 25-50 Hz. The scan resolution was 0.5 μm or less. Calcium imaging was performed in line-scan mode at 100 Hz, 20-50 pixels per neuron, and ~10 μs dwell time.

Identification of INs and PCs *in vivo* and combination of 2-photon calcium imaging and OG stimulation

First, we acquired 2-photon Z-stacks of structural reference images. Since ChR2 in the VGAT-ChR2(H134R)-EYFP line is fused with enhanced yellow fluorescent protein (EYFP) (16),

we used EYFP fluorescence to identify INs. SR101 was used to label astrocytes (80) (**Figure 3 – figure supplement 1A**). Next, we loaded cells with OGB1 within the same volume and performed *in vivo* calcium imaging in cortical layer II/III. OGB1 has a strong spectral overlap with EYFP, and, in addition, ChR2-EYFP expression in the VGAT-ChR2(H134R)-EYFP line is relatively weak. As a result, EYFP was not detectable after addition of OGB1. Therefore, we used SR101 to coregister OGB1 images with the reference (EYFP/SR101) images. EYFP-positive cells were labeled as INs, and cells negative for EYFP and SR101 were labeled as PCs (**Figure 3 – figure supplement 1B**). Data could not be acquired during OG stimulation because, despite the optical filtration, some of 473 nm excitation light reached the photodetectors causing their saturation. Therefore, we used brief (5 ms) light pulses and acquired line scans at 100 Hz (10 ms per line) limiting the light artifact to 20-30 ms. In this regime, we were in a good position to detect calcium transients that have a fast rise and slow decay (time constant ~1 s (86)).

Pharmacology

All drugs were applied topically under the objective and let to diffuse into the cortical tissue for at least 40 min. D-(-)-2-amino-5-phosphonopentanoic acid (AP5, 500 μM in ACSF, A5282, Sigma) and 6-Cyano-7-nitroquinoxaline-2,3-dione (CNQX, 200 μM in ACSF, C239, Sigma) were used to block AMPA and NMDA receptors for glutamate, respectively. Tetrodotoxin (TTX, 50 μM in ACSF, 554412, Calbiochem), was applied to block Na^+ channels required for generation and propagation of APs. N2-(Diphenylacetyl)-N-[(4-hydroxyphenyl)methyl]-D-arginine amide (BIBP 3226, 100 μM in ACSF, B174, Sigma) was applied to block Y1 receptors for NPY.

Immunofluorescence staining

679 Brains extracted from adult VGAT-ChR2(H134R)-EYFP or wild type mice were placed in
680 phosphate-buffered saline (PBS) with 4% paraformaldehyde for 12 hours at 4°C and then in
681 PBS with 30% sucrose at 4°C for 24 hours. 40 µm coronal sections were cut with a vibratome
682 (The Vibratome Company). Sections were placed in PBS with 0.5% bovine serum albumin
683 (BSA). After permeabilization with 1% Triton X-100 and 0.5% BSA in PBS for 1 h and blocking
684 with 10% normal goat serum, 0.5% BSA, and 0.1% Triton X-100 in PBS for 3 h, sections were
685 incubated overnight at 4°C with primary antibodies (anti-GAD67, mouse monoclonal clone
686 1G10.2, Millipore MAB5406; anti-EGFP, rabbit polyclonal antiserum, Abcam ab290; both diluted
687 1:1000 in blocking solution). After washing, sections were incubated with goat anti-mouse and
688 goat anti-rabbit antibodies coupled to Alexa 594 and Alexa 488 (Invitrogen A 11005 and A
689 11034), respectively, which were diluted 1:500 in blocking solution. Sections were mounted on
690 glass slides with ProLong Gold Antifade Mountant with DAPI (Invitrogen). To confirm specificity
691 of the EGFP antiserum, we stained sections from a wild type mouse. To control for unspecific
692 binding of the secondary antibodies, we incubated sections only with the secondary antibodies.
693 Stained sections were imaged on the 2-photon microscope described under “Two-Photon
694 Imaging” using 750 nm excitation, an Olympus 20x (XLUMPlanFLNXW, NA=1.0) objective and
695 460/60 nm, 525/50 nm, 670/50 nm filters to detect DAPI, Alexa 488, and Alexa 594 emissions.
696 Two-photon image stacks (Z-step size 3 µm, 1024x1024 pixel, 400x400 µm field-of-view) were
697 used to count $GAD67^+$, $EYFP^+$, or $GAD67^+/EYFP^+$ cells.
698
699 **Extracellular electrophysiological recordings**
700 Extracellular recordings of LFP and MUA were acquired as described in (50, 87, 88),
701 using a tungsten microelectrode (FHC, 6-8 MΩ). The recorded potential was amplified and
702 filtered into two signals: a low-frequency part (0.1–500 Hz, sampled at 2 kHz with 16 bits) and a
703 high-frequency part (150 –5,000 Hz, sampled at 20 kHz with 12 bits). The low-frequency part is
704 referred to as the LFP. The high-frequency part was further filtered digitally between 750 and

5,000 Hz using a zero phase-shift second-order Butterworth filter and rectified along the time axis to provide the MUA.

Microelectrodes were guided under the glass coverslip and positioned in cortical layer II/III using Luigs & Neumann translation stage (380FM-U) and manipulation equipment integrated into the Ultima system. In calcium imaging experiments, the electrode was moved into the field of view right after acquisition of the imaging data. Simultaneous 2-photon imaging and electrophysiological recordings from exactly the same location was not possible because of the photovoltaic artifact resulting from direct exposure of the metal microelectrode to focused Ti:Sapphire laser light.

Computing membrane potential in reconstructed neurons

Reconstructed neuronal morphologies were obtained from NeuroMorpho.Org (41). We used two VIP-positive cells (ID= NMO_06142, NMO_06144) from layer II/III of the rat Barrel cortex provided by Bruno Cauli (49). First, the original morphologies were scaled in Z (depth axis) by 0.6 to account for differences in the cortical thickness between the rat and mouse SI. Next, we stretched the middle dendritic section from 100 μm below the surface (the border between layers I and II) to the soma along the depth axis to position the soma in layer V (600 μm deep) approximating morphology of a VIP-positive neuron from layer V (**Figure 4 – figure supplement 2**). All computations were carried out in the Neuron simulation environment (42) assuming passive membrane properties.

Imaging data analysis

Data were analyzed in MATLAB using custom-written software as described in (13, 69). Unless indicated, statistics were performed across subjects. In scatter plots, measurements were group-averaged according to the depth in 100-μm bins for each subject before calculating

the mean and SE across subjects for each bin. P-value for the regression parameters of the scatter data, in particular, slope values for the linear regression fits, were computed using MATLAB's statistical toolbox function regstats(). The reported p-value is for the t statistic using the null hypothesis that the slope is equal to zero.

When multiple categories were defined (e.g., time-courses with and without constriction in **Figure 1B**), we averaged measurements for each category within a subject prior to performing statistics across subjects. When peak normalization was applied, we first averaged all time courses acquired within a subject. Then, averaged time courses were normalized by the peak amplitude before calculating the average across subjects.

For analysis of calcium imaging data, acquired in line-scan mode, line segments corresponding to individual neuronal cell bodies were segmented based on their intensity profile (cell bodies were brighter than neuropil). For each sampled neuron, the calcium signal per time point (i.e., one line of the line-scan) was calculated as an average of all pixels within the corresponding line segment. This calculation was repeated for each line in the time series to generate a single-neuron time-course. The same procedure was performed separately for each neuron, resulting in a family of neuron-specific time-courses for each line-scan. After digital removal of the OG light artifact, data were downsampled by a factor of two along the time axis to provide a 20-ms time resolution.

Acknowledgements

We gratefully acknowledge support from the NIH (NS057198, EB00790, U01NS094232, NS082097, EB003832 and S10RR029050), the Research Council of Norway, and the Ministry of Education, Youth and Sports of the Czech Republic (project CEITEC 2020 (LQ1601)). K. Kılıç was supported by a postdoctoral fellowship from the International Headache Society in 2014 and TUBITAK in 2015. F. Razoux, M. Thunemann and M. Desjardins were supported by postdoctoral fellowships from the Swiss National Science Foundation, German Research Council (DFG TH 2031/1) and Natural Sciences and Engineering Research Council of Canada, respectively.

References

1. Raichle ME & Mintun MA (2006) Brain work and brain imaging. *Annual review of neuroscience* 29:449-476.
2. Kleinfeld D*, et al.* (2011) A guide to delineate the logic of neurovascular signaling in the brain. *Front Neuroenergetics* 3:1.
3. Cauli B & Hamel E (2010) Revisiting the role of neurons in neurovascular coupling. *Front Neuroenergetics* 2:9.
4. Buxton RB, Griffeth VE, Simon AB, Moradi F, & Shmuel A (2014) Variability of the coupling of blood flow and oxygen metabolism responses in the brain: a problem for interpreting BOLD studies but potentially a new window on the underlying neural activity. *Frontiers in neuroscience* 8:139.
5. Lacroix A*, et al.* (2015) COX-2-Derived Prostaglandin E2 Produced by Pyramidal Neurons Contributes to Neurovascular Coupling in the Rodent Cerebral Cortex. *J Neurosci* 35(34):11791-11810.
6. Lecrux C*, et al.* (2011) Pyramidal neurons are "neurogenic hubs" in the neurovascular coupling response to whisker stimulation. *J Neurosci* 31(27):9836-9847.
7. Markram H*, et al.* (2004) Interneurons of the neocortical inhibitory system. *Nat Rev Neurosci* 5(10):793-807.
8. Cauli B*, et al.* (2004) Cortical GABA interneurons in neurovascular coupling: relays for subcortical vasoactive pathways. *J Neurosci* 24(41):8940-8949.
9. Perrenoud Q*, et al.* (2012) Activation of cortical 5-HT(3) receptor-expressing interneurons induces NO mediated vasodilatations and NPY mediated vasoconstrictions. *Front Neural Circuits* 6:50.
10. Anenberg E, Chan AW, Xie Y, LeDue JM, & Murphy TH (2015) Optogenetic stimulation of GABA neurons can decrease local neuronal activity while increasing cortical blood flow. *J Cereb Blood Flow Metab*.
11. Devor A*, et al.* (2008) Stimulus-induced changes in blood flow and 2-deoxyglucose uptake dissociate in ipsilateral somatosensory cortex. *J Neurosci* 28(53):14347-14357.
12. Devor A*, et al.* (2007) Suppressed neuronal activity and concurrent arteriolar vasoconstriction may explain negative blood oxygenation level-dependent signal. *J Neurosci* 27(16):4452-4459.
13. Tian P*, et al.* (2010) Cortical depth-specific microvascular dilation underlies laminar differences in blood oxygenation level-dependent functional MRI signal. *Proc Natl Acad Sci U S A* 107(34):15246-15251.
14. Lindvere L*, et al.* (2013) Cerebral microvascular network geometry changes in response to functional stimulation. *Neuroimage* 71:248-259.
15. Sokoloff L*, et al.* (1977) The [14C]deoxyglucose method for the measurement of local cerebral glucose utilization: theory, procedure, and normal values in the conscious and anesthetized albino rat. *J Neurochem* 28(5):897-916.
16. Zhao S*, et al.* (2011) Cell type-specific channelrhodopsin-2 transgenic mice for optogenetic dissection of neural circuitry function. *Nat Methods* 8(9):745-752.
17. Doronin A & Meglinski I (2011) Online object oriented Monte Carlo computational tool for the needs of biomedical optics. *Biomed Opt Express* 2(9):2461-2469.
18. Doronin A & Meglinski I (2012) Peer-to-peer Monte Carlo simulation of photon migration in topical applications of biomedical optics. *J Biomed Opt* 17(9):90504-90501.
19. Yona G, Meitav N, Kahn I, & Shoham S (2016) Realistic Numerical and Analytical Modeling of Light Scattering in Brain Tissue for Optogenetic Applications(1,2,3). *eNeuro* 3(1).

20. Aravanis AM*, et al.* (2007) An optical neural interface: in vivo control of rodent motor cortex with integrated fiberoptic and optogenetic technology. *Journal of neural engineering* 4(3):S143-156.
21. Foutz TJ, Arlow RL, & McIntyre CC (2012) Theoretical principles underlying optical stimulation of a channelrhodopsin-2 positive pyramidal neuron. *J Neurophysiol* 107(12):3235-3245.
22. Christie IN*, et al.* (2012) fMRI response to blue light delivery in the naive brain: Implications for combined optogenetic fMRI studies. *Neuroimage* 66C:634-641.
23. Bean BP (2007) The action potential in mammalian central neurons. *Nat Rev Neurosci* 8(6):451-465.
24. de la Pena E & Geijo-Barrientos E (1996) Laminar localization, morphology, and physiological properties of pyramidal neurons that have the low-threshold calcium current in the guinea-pig medial frontal cortex. *J Neurosci* 16(17):5301-5311.
25. Buzsaki G, Anastassiou CA, & Koch C (2012) The origin of extracellular fields and currents--EEG, ECoG, LFP and spikes. *Nat Rev Neurosci* 13(6):407-420.
26. Einevoll GT, Kayser C, Logothetis NK, & Panzeri S (2013) Modelling and analysis of local field potentials for studying the function of cortical circuits. *Nat Rev Neurosci* 14(11):770-785.
27. Buzsaki G (2004) Large-scale recording of neuronal ensembles. *Nat Neurosci* 7(5):446-451.
28. Einevoll GT, Franke F, Hagen E, Pouzat C, & Harris KD (2012) Towards reliable spike-train recordings from thousands of neurons with multielectrodes. *Curr Opin Neurobiol* 22(1):11-17.
29. Pettersen KH & Einevoll GT (2008) Amplitude variability and extracellular low-pass filtering of neuronal spikes. *Biophys J* 94(3):784-802.
30. Grewe BF, Langer D, Kasper H, Kampa BM, & Helmchen F (2010) High-speed in vivo calcium imaging reveals neuronal network activity with near-millisecond precision. *Nat Methods* 7(5):399-405.
31. Pnevmatikakis EA*, et al.* (2016) Simultaneous Denoising, Deconvolution, and Demixing of Calcium Imaging Data. *Neuron* 89(2):285-299.
32. Yaksi E & Friedrich RW (2006) Reconstruction of firing rate changes across neuronal populations by temporally deconvolved Ca2+ imaging. *Nat Methods* 3(5):377-383.
33. Stosiek C, Garaschuk O, Holthoff K, & Konnerth A (2003) In vivo two-photon calcium imaging of neuronal networks. *Proc Natl Acad Sci U S A* 100(12):7319-7324.
34. Langer D & Helmchen F (2012) Post hoc immunostaining of GABAergic neuronal subtypes following in vivo two-photon calcium imaging in mouse neocortex. *Pflugers Arch* 463(2):339-354.
35. Kerlin AM, Andermann ML, Berezovskii VK, & Reid RC (2010) Broadly tuned response properties of diverse inhibitory neuron subtypes in mouse visual cortex. *Neuron* 67(5):858-871.
36. Beltramo R*, et al.* (2013) Layer-specific excitatory circuits differentially control recurrent network dynamics in the neocortex. *Nat Neurosci* 16(2):227-234.
37. Merighi A, Salio C, Ferrini F, & Lossi L (2011) Neuromodulatory function of neuropeptides in the normal CNS. *Journal of chemical neuroanatomy* 42(4):276-287.
38. Schoenenberger P, Grunditz A, Rose T, & Oertner TG (2008) Optimizing the spatial resolution of Channelrhodopsin-2 activation. *Brain Cell Biol* 36(1-4):119-127.
39. Kawaguchi Y & Kubota Y (1996) Physiological and morphological identification of somatostatin- or vasoactive intestinal polypeptide-containing cells among GABAergic cell subtypes in rat frontal cortex. *J Neurosci* 16(8):2701-2715.
40. Cauli B, Zhou X, Tricoire L, Toussay X, & Staiger JF (2014) Revisiting enigmatic cortical calretinin-expressing interneurons. *Frontiers in neuroanatomy* 8:52.

41. Ascoli GA, Donohue DE, & Halavi M (2007) NeuroMorpho.Org: a central resource for neuronal morphologies. *J Neurosci* 27(35):9247-9251.
42. Hines ML & Carnevale NT (1997) The NEURON simulation environment. *Neural computation* 9(6):1179-1209.
43. Nagel G*, et al.* (2003) Channelrhodopsin-2, a directly light-gated cation-selective membrane channel. *Proc Natl Acad Sci U S A* 100(24):13940-13945.
44. Neske GT, Patrick SL, & Connors BW (2015) Contributions of diverse excitatory and inhibitory neurons to recurrent network activity in cerebral cortex. *J Neurosci* 35(3):1089-1105.
45. Arenkiel BR*, et al.* (2007) In vivo light-induced activation of neural circuitry in transgenic mice expressing channelrhodopsin-2. *Neuron* 54(2):205-218.
46. Dacey RG, Jr., Bassett JE, & Takayasu M (1988) Vasomotor responses of rat intracerebral arterioles to vasoactive intestinal peptide, substance P, neuropeptide Y, and bradykinin. *J Cereb Blood Flow Metab* 8(2):254-261.
47. Abounader R*, et al.* (1999) Expression of neuropeptide Y receptors mRNA and protein in human brain vessels and cerebromicrovascular cells in culture. *J Cereb Blood Flow Metab* 19(2):155-163.
48. Bao L*, et al.* (1997) Localization of neuropeptide Y Y1 receptors in cerebral blood vessels. *Proc Natl Acad Sci U S A* 94(23):12661-12666.
49. Karagiannis A*, et al.* (2009) Classification of NPY-expressing neocortical interneurons. *J Neurosci* 29(11):3642-3659.
50. Devor A*, et al.* (2005) Coupling of the cortical hemodynamic response to cortical and thalamic neuronal activity. *Proc Natl Acad Sci U S A* 102(10):3822-3827.
51. Helmstaedter M, Sakmann B, & Feldmeyer D (2009) Neuronal correlates of local, lateral, and translaminar inhibition with reference to cortical columns. *Cereb Cortex* 19(4):926-937.
52. Stuart GJ & Sakmann B (1994) Active propagation of somatic action potentials into neocortical pyramidal cell dendrites. *Nature* 367(6458):69-72.
53. Goldberg JH, Tamas G, & Yuste R (2003) Ca2+ imaging of mouse neocortical interneurone dendrites: Ia-type K+ channels control action potential backpropagation. *J Physiol* 551(Pt 1):49-65.
54. Kaiser KM, Zilberter Y, & Sakmann B (2001) Back-propagating action potentials mediate calcium signalling in dendrites of bitufted interneurons in layer 2/3 of rat somatosensory cortex. *J Physiol* 535(Pt 1):17-31.
55. Cho KH*, et al.* (2010) Subtype-specific dendritic Ca(2+) dynamics of inhibitory interneurons in the rat visual cortex. *J Neurophysiol* 104(2):840-853.
56. Gordon GR, Choi HB, Rungta RL, Ellis-Davies GC, & MacVicar BA (2008) Brain metabolism dictates the polarity of astrocyte control over arterioles. *Nature* 456(7223):745-749.
57. Liu X, Li C, Falck JR, Harder DR, & Koehler RC (2012) Relative contribution of cyclooxygenases, epoxyeicosatrienoic acids, and pH to the cerebral blood flow response to vibrissal stimulation. *Am J Physiol Heart Circ Physiol* 302(5):H1075-1085.
58. Perrenoud Q*, et al.* (2012) Characterization of Type I and Type II nNOS-Expressing Interneurons in the Barrel Cortex of Mouse. *Front Neural Circuits* 6:36.
59. Segal SS & Duling BR (1986) Flow control among microvessels coordinated by intercellular conduction. *Science* 234(4778):868-870.
60. Rosenblum WI, Weinbrecht P, & Nelson GH (1990) Propagated constriction in mouse pial arterioles: possible role of endothelium in transmitting the propagated response. *Microcirc Endothelium Lymphatics* 6(4-5):369-387.
61. Jensen LJ & Holstein-Rathlou NH (2013) The vascular conducted response in cerebral blood flow regulation. *J Cereb Blood Flow Metab* 33(5):649-656.

62. Chen BR, Kozberg MG, Bouchard MB, Shaik MA, & Hillman EM (2014) A critical role for the vascular endothelium in functional neurovascular coupling in the brain. *Journal of the American Heart Association* 3(3):e000787.
63. Peppiatt CM, Howarth C, Mobbs P, & Attwell D (2006) Bidirectional control of CNS capillary diameter by pericytes. *Nature* 443(7112):700-704.
64. Welsh DG & Segal SS (1998) Endothelial and smooth muscle cell conduction in arterioles controlling blood flow. *Am J Physiol* 274(1 Pt 2):H178-186.
65. Iadecola C, Yang G, Ebner TJ, & Chen G (1997) Local and propagated vascular responses evoked by focal synaptic activity in cerebellar cortex. *J Neurophysiol* 78(2):651-659.
66. Chen BR, Bouchard MB, McCaslin AF, Burgess SA, & Hillman EM (2011) High-speed vascular dynamics of the hemodynamic response. *Neuroimage* 54(2):1021-1030.
67. Siero JC, Petridou N, Hoogduin H, Luijten PR, & Ramsey NF (2011) Cortical depth-dependent temporal dynamics of the BOLD response in the human brain. *J Cereb Blood Flow Metab* 31(10):1999-2008.
68. Yu X, Qian C, Chen DY, Dodd SJ, & Koretsky AP (2014) Deciphering laminar-specific neural inputs with line-scanning fMRI. *Nat Methods* 11(1):55-58.
69. Nizar K*, et al.* (2013) In vivo Stimulus-Induced Vasodilation Occurs without IP3 Receptor Activation and May Precede Astrocytic Calcium Increase. *J Neurosci* 33(19):8411-8422.
70. Bonder DE & McCarthy KD (2014) Astrocytic Gq-GPCR-linked IP3R-dependent Ca2+ signaling does not mediate neurovascular coupling in mouse visual cortex in vivo. *J Neurosci* 34(39):13139-13150.
71. Takata N*, et al.* (2013) Cerebral blood flow modulation by Basal forebrain or whisker stimulation can occur independently of large cytosolic Ca2+ signaling in astrocytes. *PLoS One* 8(6):e66525.
72. Jego P, Pacheco-Torres J, Araque A, & Canals S (2014) Functional MRI in mice lacking IP3-dependent calcium signaling in astrocytes. *J Cereb Blood Flow Metab* 34(10):1599-1603.
73. Tasic B*, et al.* (2016) Adult mouse cortical cell taxonomy revealed by single cell transcriptomics. *Nat Neurosci* 19(2):335-346.
74. Cahoy JD*, et al.* (2008) A transcriptome database for astrocytes, neurons, and oligodendrocytes: a new resource for understanding brain development and function. *J Neurosci* 28(1):264-278.
75. Attwell D & Laughlin SB (2001) An energy budget for signaling in the grey matter of the brain. *J Cereb Blood Flow Metab* 21(10):1133-1145.
76. Attwell D & Iadecola C (2002) The neural basis of functional brain imaging signals. *Trends Neurosci* 25(12):621-625.
77. Davis TL, Kwong KK, Weisskoff RM, & Rosen BR (1998) Calibrated functional MRI: mapping the dynamics of oxidative metabolism. *Proc Natl Acad Sci U S A* 95(4):1834-1839.
78. Hoge RD (2012) Calibrated FMRI. *Neuroimage* 62(2):930-937.
79. Pike GB (2012) Quantitative functional MRI: concepts, issues and future challenges. *Neuroimage* 62(2):1234-1240.
80. Nimmerjahn A, Kirchhoff F, Kerr JN, & Helmchen F (2004) Sulforhodamine 101 as a specific marker of astroglia in the neocortex in vivo. *Nat Methods* 1(1):31-37.
81. Shin HK*, et al.* (2007) Age-dependent cerebrovascular dysfunction in a transgenic mouse model of cerebral amyloid angiopathy. *Brain : a journal of neurology* 130(Pt 9):2310-2319.
82. Drew PJ*, et al.* (2010) Chronic optical access through a polished and reinforced thinned skull. *Nat Methods* 7(12):981-984.

83. Flock ST, Jacques SL, Wilson BC, Star WM, & van Gemert MJ (1992) Optical properties of Intralipid: a phantom medium for light propagation studies. *Lasers in surgery and medicine* 12(5):510-519.
84. Pisanello F*, et al.* (2014) Multipoint-emitting optical fibers for spatially addressable in vivo optogenetics. *Neuron* 82(6):1245-1254.
85. Kobat D*, et al.* (2009) Deep tissue multiphoton microscopy using longer wavelength excitation. *Opt Express* 17(16):13354-13364.
86. Lutcke H, Gerhard F, Zenke F, Gerstner W, & Helmchen F (2013) Inference of neuronal network spike dynamics and topology from calcium imaging data. *Front Neural Circuits* 7:201.
87. Devor A*, et al.* (2003) Coupling of total hemoglobin concentration, oxygenation, and neural activity in rat somatosensory cortex. *Neuron* 39(2):353-359.
88. Einevoll GT*, et al.* (2007) Laminar population analysis: estimating firing rates and evoked synaptic activity from multielectrode recordings in rat barrel cortex. *J Neurophysiol* 97(3):2174-2190.

Figure Legends

Figure 1. Sensory stimulus-induced arteriolar response

A. An example vascular image stack throughout the cortical depth. Three 50-μm slabs at different depths are shown. Red arrows indicate the direction of flow in a surface arteriole diving at 3 points.

B. Sensory stimulus-induced dilation time-courses sorted into two categories by the presence or absence of the constriction phase, defined as the peak constriction amplitude exceeding 1%. The black curve (constriction): n = 419 measurements, 34 subjects. The red curve (no constriction): n = 397 measurements, 47 subjects. Error bars indicate standard error (SE) across subjects.

C. Onset (black) and time-to-peak (red) of dilation as a function of depth. Each data point represents a single measurement. For each subject, the data were group-averaged according to depth in 100-μm bins. Error bars represent the mean ± SE across subjects for each bin (green).

D. A zoomed-in view onto the initial eight seconds of the response. Time-courses were grouped by depth as in (C) and peak-normalized (see **Materials and methods**) to facilitate visual inspection of temporal differences. Color-coded depth categories are indicated on top.

Figure 1 – figure supplement 1. Sensory stimulus-induced arteriolar response – additional quantification

A. Constriction amplitude (in % change) as a function of depth for cases with peak constriction > 1%. Each data point represents a single measurement. For each subject, the data were group-averaged according to depth in 100-μm bins. Error bars represent the mean ± SE across subjects (green).

B. Dilation amplitude (in % change) as a function of depth. Conventions are as in (A).

C. As in **Figure 1D** without peak normalization. Error bars represent SE across subjects.

Figure 2. Arteriolar response to OG stimulation of INs

A. Left: The 473-nm laser beam visualized in fluorescent medium. Right: Schematic illustration of the OG beam centered on a diving arteriole. The full width at half maximum (FWHM = 230 μm) of the beam is superimposed on a mean intensity projection (MIP) of a 2-photon image stack of FITC-labeled vasculature through the top 116 μm. Individual images were acquired every 3 μm. Red arrows indicate the direction of flow in the arteriole.

B. Simulated spatial profile of the OG beam in cortical tissue. Top: Color-coded photon density. Bottom: Photon density as a function of depth (z-axis) and as a function of the radial distance (r) at three different depths (75, 225, and 425 μm).

C. Left: An example vascular MIP throughout the top 180 μm. Right: the measurement plane 180 μm deep including intravascular FITC (green) and SR101-labeled astrocytes (red). The white line indicates the scanning trajectory used for diameter measurements in (D).

D. Diameter change time-courses of the diving arteriole in (C) in response to the sensory and OG stimuli (sensory: black, average of 10 stimulus trials; OG: red, single trial).

E. Each thin gray line shows an average response within one subject. Across-subject average is overlaid in thick black. Error bars indicate SE across subjects. The mean peak dilation, peak constriction, and the ratio of peak dilation to peak constriction are shown in the inset. Error bars indicate SE across subjects.

F. Averaged dilation time-courses grouped by depth. An expanded view of the initial 4 seconds after the stimulus onset is shown. The depth in μm is indicated on the left. Error bars indicate SE across subjects.

G. Dilation onset (black) and time-to-peak (red) as a function of depth. Conventions are as in **Figure 1C**.

H. As in (G) for constriction onset (see text).

Figure 2 – figure supplement 1. GAD67/ChR2-EYFP immunostaining of the cortex from a VGAT-ChR2(H134R)-EYFP mouse

Coronal brain sections were incubated with GAD67 antibodies, which detect the GABA-producing enzyme glutamate decarboxylase (GAD) expressed in INs, and with EGFP antiserum to detect the membrane-targeted ChR2-EYFP fusion protein. Secondary antibodies coupled to Alexa 594 (red) and Alexa 488 (green) were used to detect the respective primary antibodies. DAPI was used to visualize cell nuclei (blue). Two-photon image stacks were acquired using 750-nm excitation. We counted 299 ChR2-EYFP+ (96%) and 12 ChR2-EYFP$^-$ (4%) neurons out of 311 GAD67$^+$ neurons in 12 representative images. We did not detect GAD67$^-$/ChR2-EYFP$^+$ neurons. The arrowhead in the right panel is pointing towards a GAD67$^+$/ChR2-EYFP$^-$ neuron.

Figure 2 – figure supplement 2. Arteriolar response to OG stimulation of INs – additional quantification

A. The OG response as a function of varying the duration of the light stimulus at constant power. Each curve corresponds to an average of 3 subjects. Error bars indicate SE across subjects.

B. As in (A) for the stimulus power at constant stimulus duration.

C. As in **Figure 2F** but peak-normalized.

D. OG dilation amplitude (in % change) as a function of depth. Each data point represents a single measurement. For each subject, the data were group-averaged according to depth in 100-μm bins. Error bars represent the mean ± SE across subjects for each bin (green).

Figure 3. Lack of excitatory recruitment upon OG stimulation of INs

A. Top: Corresponding MUA (black) and LFP (red) recorded from layer II/III during a 200 ms OG stimulus. Each trace shows a single stimulus trial; red traces show the average of four individual

trials.

B. As in (A) for a 1 s long OG stimulus.

Figure 3 – figure supplement 1. Lack of excitatory recruitment upon OG stimulation of INs – additional evidence from calcium imaging

A. Example reference image stacks showing EYFP, SR101, and composite EYFP/SR101 fluorescence for later coregistration with OGB1/SR101 images.

B. Top: an example OGB1 image with a line-scan trajectory (the yellow curve) used to acquire calcium imaging data. The trajectory passes through a number of PCs (PC1-PC3) and INs (IN1-IN2). Below: the corresponding SR101 and composite EYFP/SR101 images used to define astrocytes (A1-A3) and INs, respectively.

C. Example calcium signal time-courses from PCs (left) and INs (right) in response to 5 ms OG stimulus (indicated by vertical lines). Each horizontal line (1-12) corresponds to a PC/IN pair that was acquired simultaneously. The average for each cell type (PCs and INs) is shown at the bottom in red.

D. MUA acquired under the same stimulus conditions. The electrode was moved into the field-of-view right after acquisition of the calcium imaging data.

Figure 3 – figure supplement 2. Lack of excitatory recruitment upon OG stimulation of INs – additional pharmacological evidence

Averaged dilation time-courses in response to OG stimulus before and after blocking glutamatergic synaptic transmission. The response under control condition (black) and after application of AMPA and NMDA receptor blockers (500 μM AP5 + 200 μM CNQX, red) are overlaid. Error bars indicate SD across measurement locations within a single subject. Under glutamatergic blockade, we observed a trend towards delayed constriction (peaking at 19.9 ± 2.0 s and 21.8 ± 2.6 s before and after the blockade, respectively). This trend, however, was not

statistically significant (P = 0.6).

Figure 4. The effect of OG stimulation of INs delivered directly to layer V

A. Representative images of EYFP-expressing INs at different depths (green – INs labeled with EYFP, red – astrocytes labeled with SR101).

B. Arteriolar response to OG stimulation of INs through the objective before and after TTX (black and red curves, respectively). Error bars indicate SE across subjects.

C. As in (B) for OG stimulation through the optical fiber with the tip in layer V. The inset shows the light-emitting fiber tip visualized in fluorescent medium.

D. Left: Example morphology of VIP-positive inhibitory neuron (ID= NMO_06142, NeuroMorpho.org). The red double ended arrow indicates the dendritic section that was stretched to approximate layer V neuron (see **Materials and methods**). Right: dendritic (top) and somatic (bottom) membrane potential in response to voltage clamping the top 50-, 100- or 150-μm of the dendritic tree at 0 mV.

E. Comparison of the arteriolar response (across-subject average) to OG stimulation of INs through the objective (black) and fiber (red). Error bars represent SE across subjects. The inset shows the mean laser power for each category (left) and a zoomed-in view onto the initial 4 seconds after the stimulus onset of the response normalized by the laser power (right).

Figure 4 – figure supplement 1. Simulation of the somatic membrane potential – another example

Left: Example neuronal morphology (ID= NMO_06144, NeuroMorpho.org). The red double ended arrow indicates dendritic section that was stretched to approximate layer V neuron (see **Materials and methods**). Right: dendritic (top) and somatic (bottom) membrane potential in response to voltage clamping the top 50-, 100- or 150-μm of the dendritic tree at 0 mV.

Figure 4 – figure supplement 2. Approximation of neuronal morphologies

A. Original morphology of layer II/III VPI-positive neuron from rat SI obtained from NeuroMorpho.org (ID= NMO_06142).

B. Scaling the morphology to approximate a mouse layer II/III neuron.

C. Stretching the middle dendritic section to approximate a mouse layer V neuron.

Figure 5. Neurovascular mechanism of the constriction phase

A. Arteriolar response to OG stimulation of PCs in Thy1-ChR2-YFP subjects before (black) and after (red) application of AMPA/NMDA glutamatergic blockers (black and red, respectively). Error bars represent SE across subjects. The inset shows the sensory response before and after drug application (500 μM AP5 + 200 μM CNQX).

B. Comparison of dilation time-courses in response to OG stimulation of INs in VGAT-ChR2(H134R)-EYFP subjects before (black) and after (red) blocking Y1 receptors for NPY with topical application of 100 μM of BIBP 3226. Error bars represent SE across subjects.

C. As in (B) for the sensory response. The data were grouped according to the presence of the constriction phase as in **Figure 1B**.

Figure 6. Imaging arteriolar response to sensory and OG stimulation of INs in awake mice

A. Arteriolar dilation in awake mice in response to a sensory stimulus (three 100-ms air puffs to the contralateral whisker pad, top panel) and OG stimulation of INs (bottom panel). Thin gray lines represent individual subjects. Across-subject averages are overlaid (thick black and red lines for the sensory and OG stimuli, respectively).

B. Overlaid dilation time-courses in response to sensory stimulation (black) and OG stimulation of INs (red). Error bars represent SE across subjects. The inset shows the same time-courses normalized to the peak.

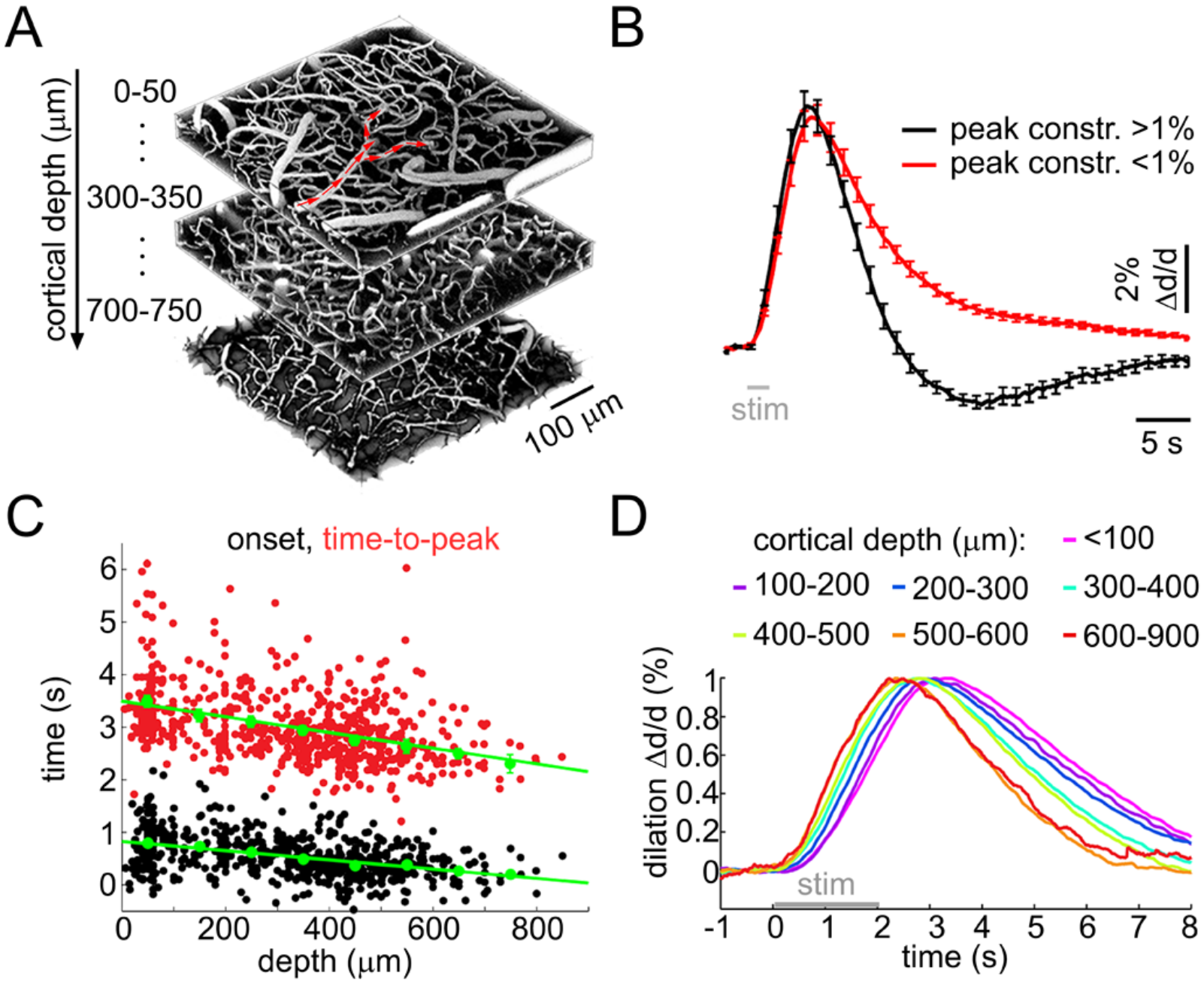
A
cortical depth (μm)
0-50
300-350
700-750
100 μm
B
peak constr. >1%
peak constr. <1%
2% Δd/d
stim
5 s
C
onset, time-to-peak
time (s)
depth (μm)
0
200
400
600
800
0
1
2
3
4
5
6
D
cortical depth (μm):
<100
100-200
200-300
300-400
400-500
500-600
600-900
dilation Δd/d (%)
stim
time (s)
-1
0
1
2
3
4
5
6
7
8
0
0.2
0.4
0.6
0.8
1

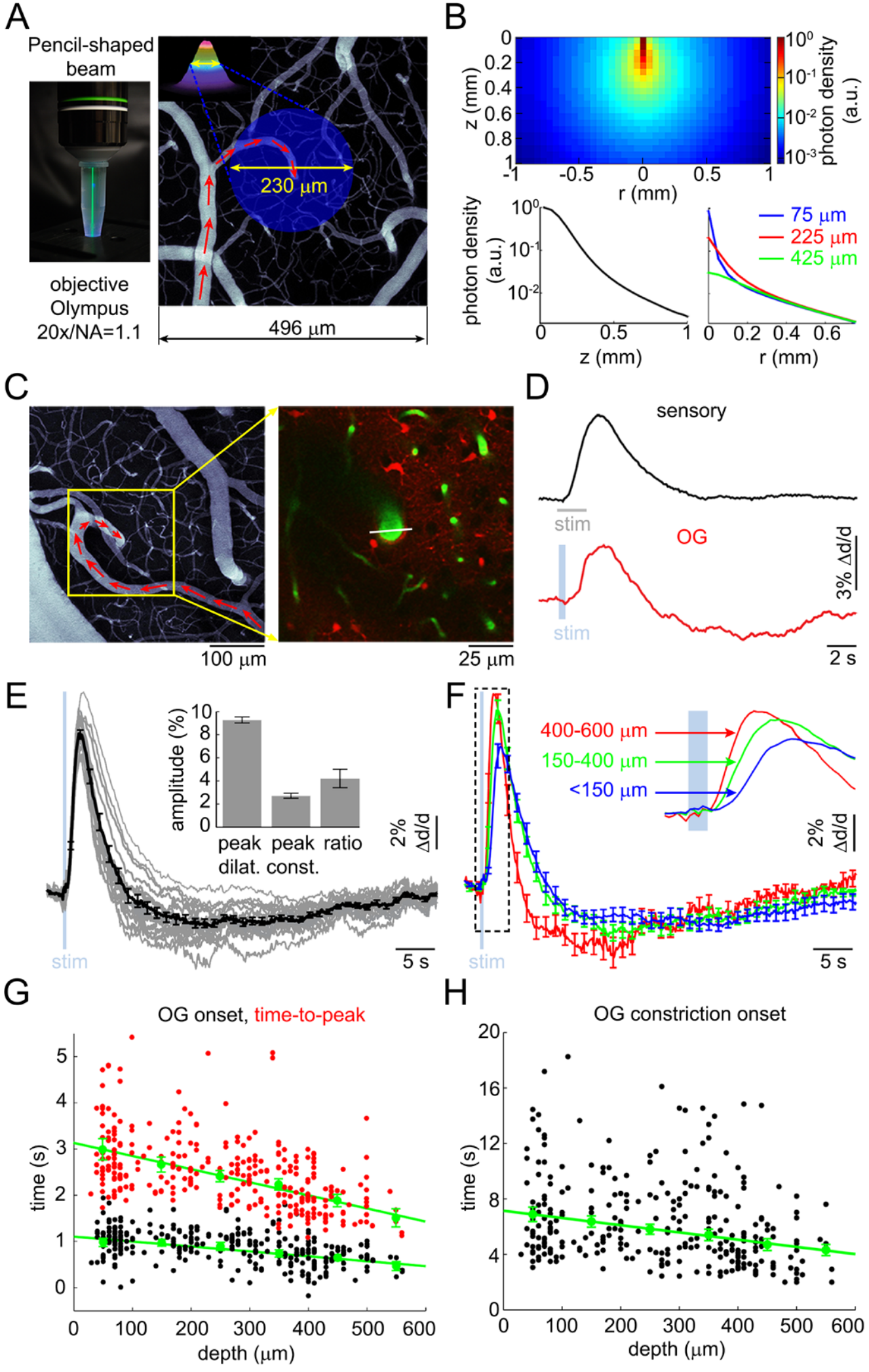
A
Pencil-shaped beam
objective Olympus 20x/NA=1.1
230 μm
496 μm
B
z (mm)
r (mm)
photon density (a.u.)
75 μm
225 μm
425 μm
C
100 μm
25 μm
D
sensory
stim
OG
3% Δd/d
2 s
E
amplitude (%)
peak dilat.
peak const.
ratio
2% Δd/d
stim
5 s
F
400-600 μm
150-400 μm
<150 μm
2% Δd/d
stim
5 s
G
OG onset, time-to-peak
time (s)
depth (μm)
H
OG constriction onset
time (s)
depth (μm)

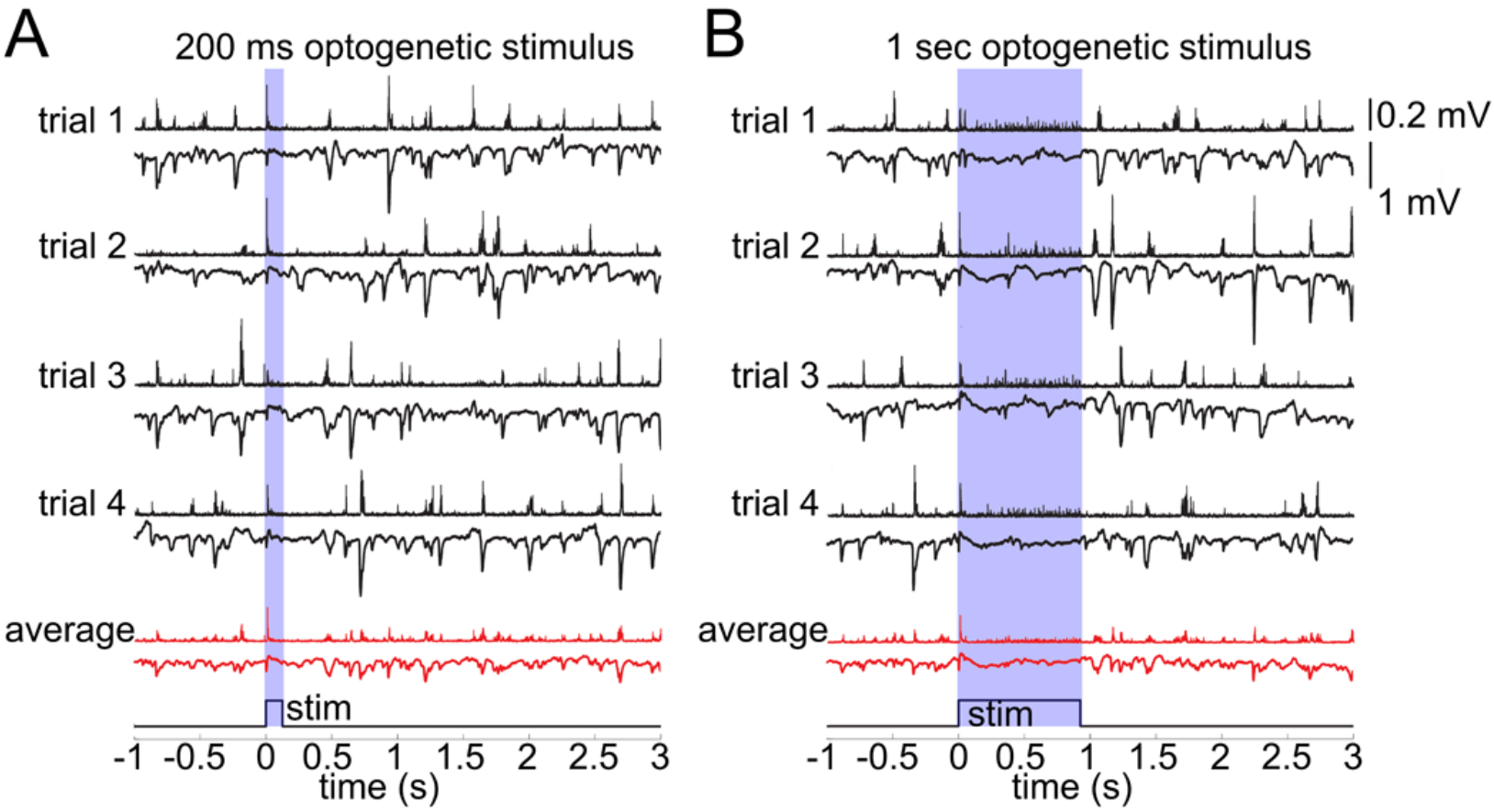
A
200 ms optogenetic stimulus
trial 1
trial 2
trial 3
trial 4
average
stim
-1 -0.5 0 0.5 1 1.5 2 2.5 3
time (s)
B
1 sec optogenetic stimulus
trial 1
trial 2
trial 3
trial 4
average
stim
0.2 mV
1 mV
-1 -0.5 0 0.5 1 1.5 2 2.5 3
time (s)

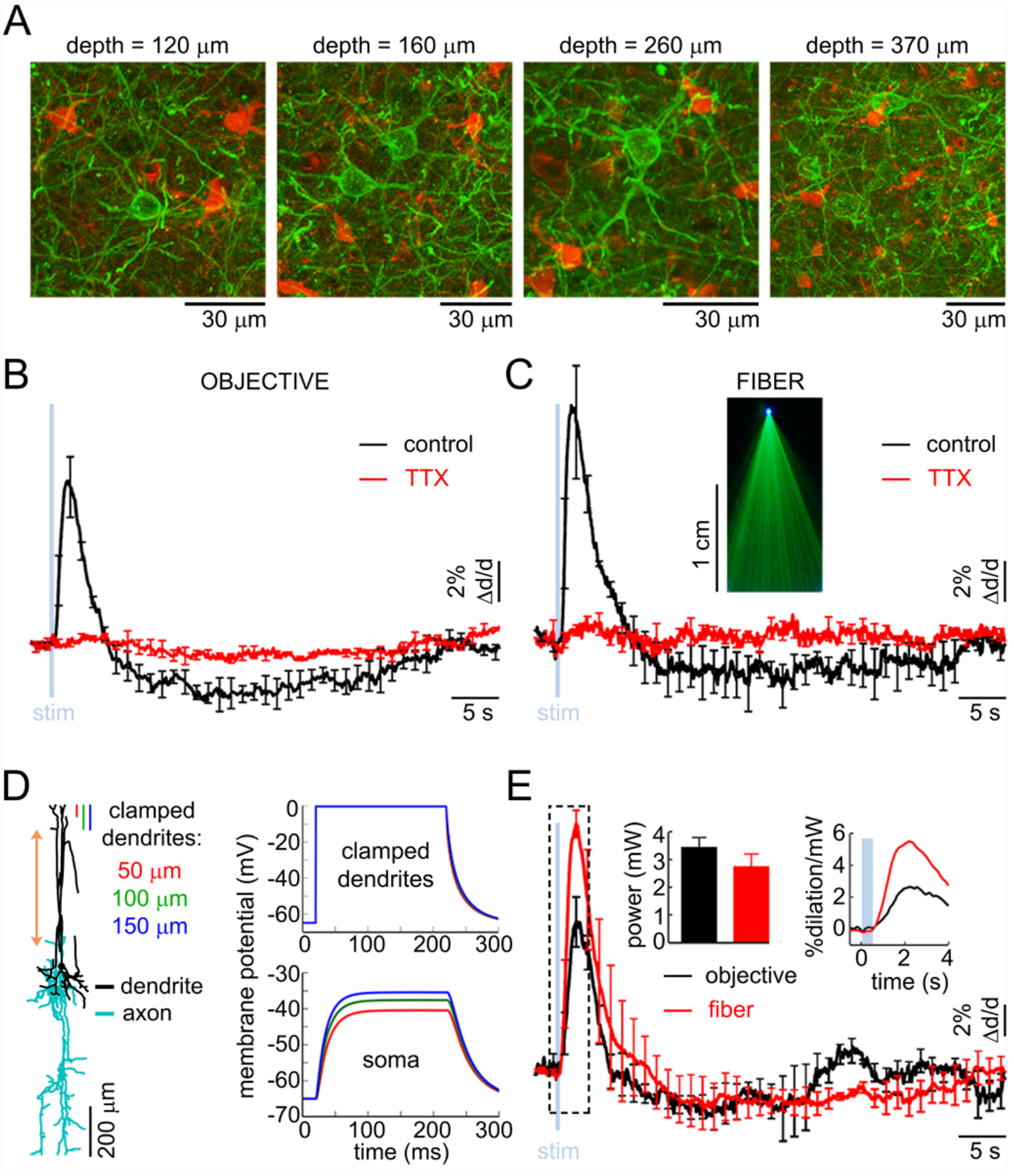
A
depth = 120 μm
depth = 160 μm
depth = 260 μm
depth = 370 μm
30 μm
30 μm
30 μm
30 μm
B
OBJECTIVE
control
TTX
2% Δd/d
stim
5 s
C
FIBER
1 cm
control
TTX
2% Δd/d
stim
5 s
D
clamped dendrites:
50 μm
100 μm
150 μm
dendrite
axon
200 μm
clamped dendrites
soma
membrane potential (mV)
time (ms)
E
power (mW)
objective
fiber
%dilation/mW
time (s)
2% Δd/d
stim
5 s

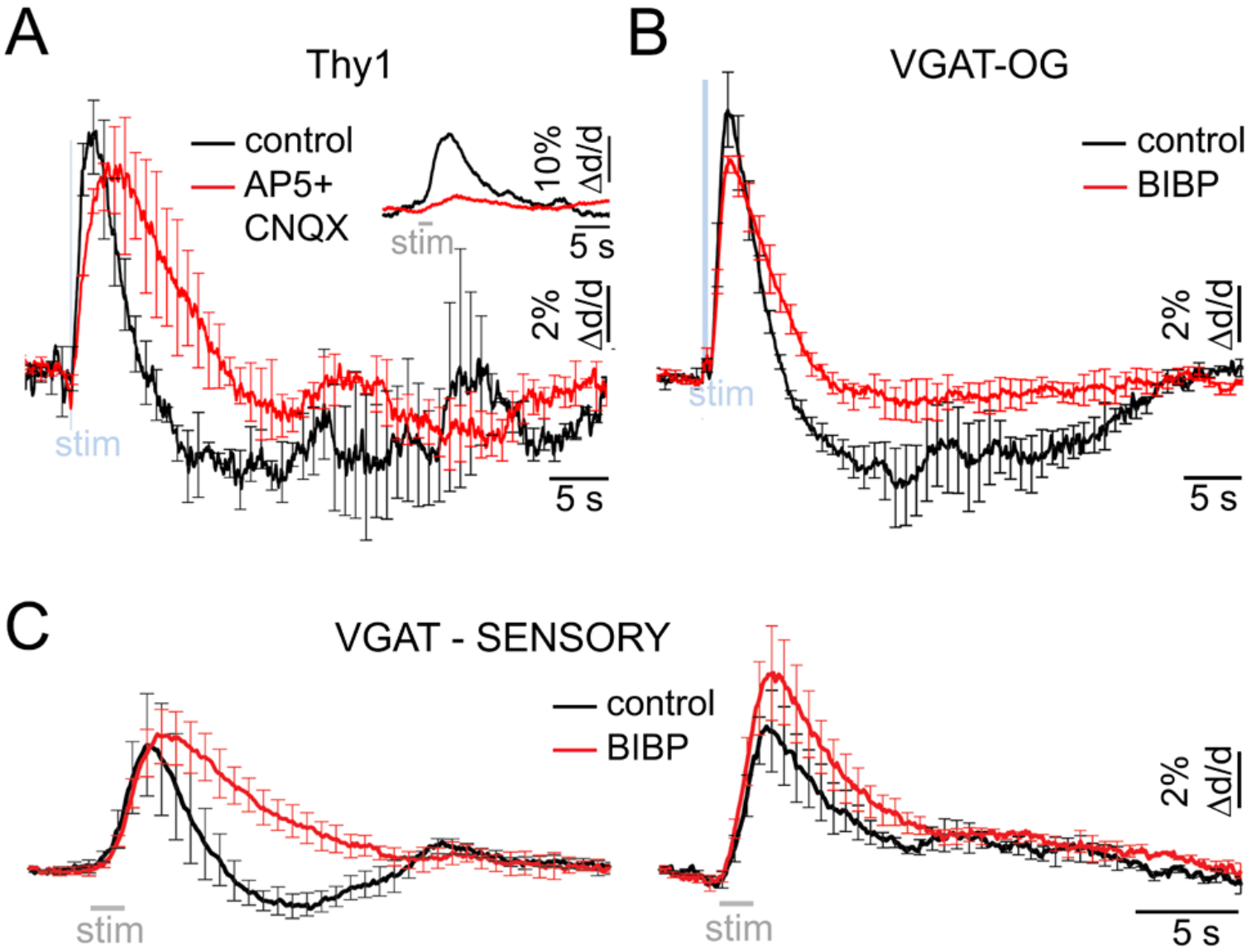
A
Thy1
control
AP5+
CNQX
10%
Δd/d
5 s
stim
2%
Δd/d
stim
5 s
B
VGAT-OG
control
BIBP
2%
Δd/d
stim
5 s
C
VGAT - SENSORY
control
BIBP
stim
2%
Δd/d
stim
5 s

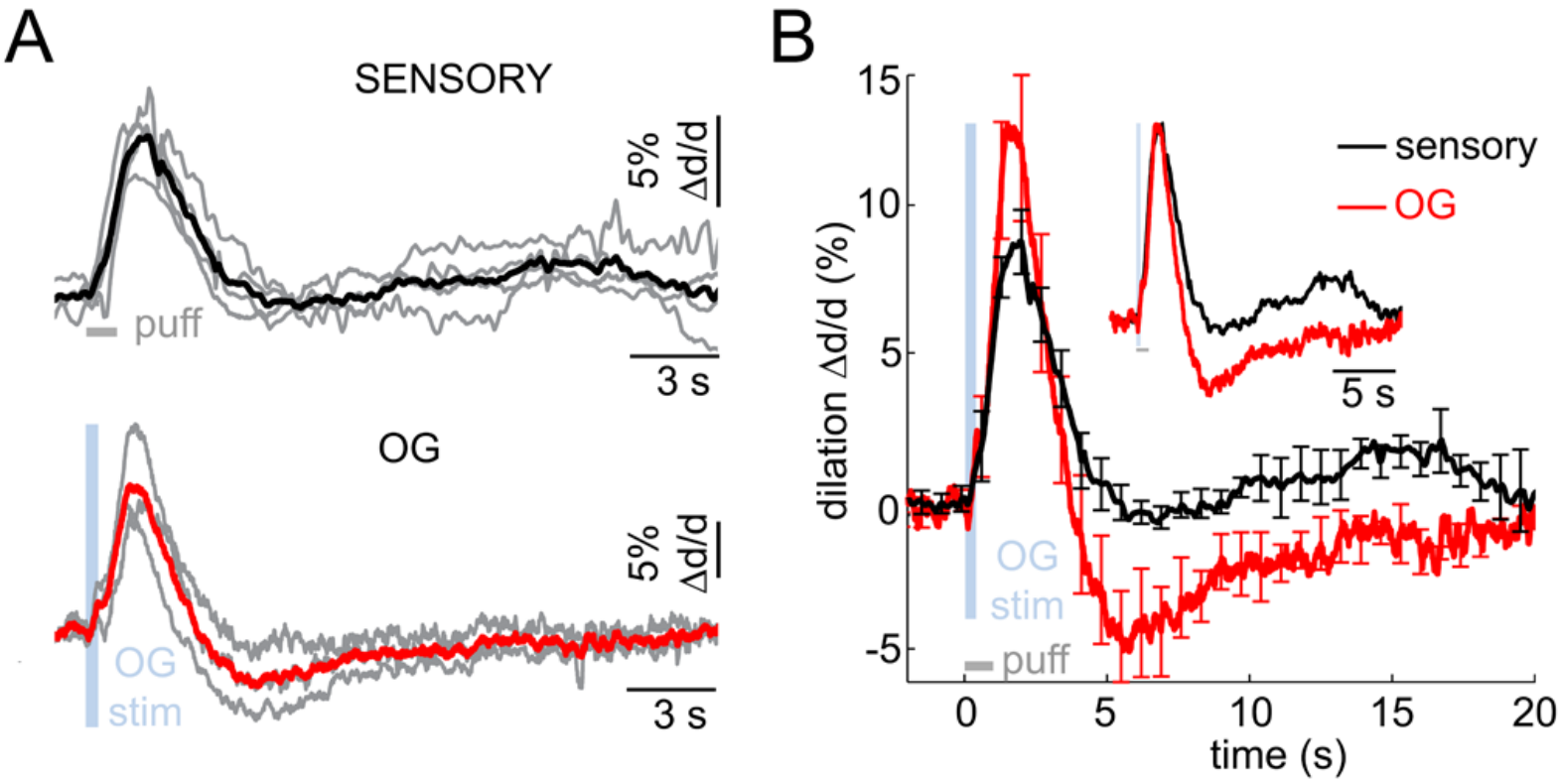
A
SENSORY
5% Δd/d
puff
3 s
OG
5% Δd/d
OG stim
3 s
B
dilation Δd/d (%)
15
10
5
0
-5
sensory
OG
5 s
OG stim
puff
0
5
10
15
20
time (s)